Cam-Clay plasticity. Part IX: On the anisotropy, heterogeneity, and viscoplasticity of shale

Ronaldo I. Borja[1,*] · Qing Yin[1] · Yang Zhao[1]

[1]Department of Civil and Environmental Engineering, Stanford University, Stanford, CA 94305, USA. *E-mail: borja@stanford.edu

Summary. We investigate three aspects of material behavior in this ninth installment of the Cam-Clay series, namely, anisotropy, heterogeneity, and viscoplasticity. The main focus of the paper is creep in shale and how this time-dependent deformation behavior may be quantified across the scales, from nanometers to millimeters. Recognizing the highly heterogeneous nature of shale, we adopt a simplified representation of this material as a mixture of softer matter representing organics and clay, and harder matter representing the inorganic rock matrix. Due to the presence of bedding planes in the rock matrix, anisotropy in both the elastic and inelastic responses is assumed; however, the superimposed softer matter may be taken to be isotropic unless experimental evidence indicates otherwise. Viscoplasticity is considered for the first time in this series of work, in which both the Duvaut-Lions and Perzyna formulations are utilized. The two viscoplastic formulations are shown to predict very similar time-dependent deformation responses. The framework is used to interpret the results of multiscale triaxial laboratory creep tests in organic-rich Barnett shale. Time-dependent strain localization in the form of dilative shear bands is also shown to result from loading with varying strain rates, as well as from creep processes that accommodate the multiscale heterogeneity of shale.

Keywords

Cam-Clay, creep, heterogeneity, shale, transverse isotropy, viscoplasticity

1 Introduction

Shale is a highly heterogeneous sedimentary rock composed of softer materials such as clay and organics, stiffer minerals such as quartz, feldspar, and pyrite, and micron- to submicron-scale pores and fractures. Unlike crystalline rocks that tend to fracture extensively under deformation [62, 63], shales can deform in a more ductile manner and has the ability to heal fractures, making them suitable for use as a seal rock [8]. For this reason, sequences of crystalline

rocks and thick shale formations have long been considered as prime storage sites for toxic waste containment, with the crystalline rock providing strength and the shale serving as a seal [1]. Shales are also known to exhibit ductile creep [58], and are found to be diverse in composition. Specifically, the type of clay and organics vary among different shales, as does the presence of other constituents, such as carbonates, smectite, pyrite, and other inclusions [8, 38, 51, 64].

Anisotropy is a prominent property of shales that is associated with the parallel alignment of clay platelets in the direction of the bedding plane [8, 17, 18, 52, 54, 68, 72, 74]. The preferential orientation of particles is attributed to deposition, compaction, and/or diagenetic processes [5, 27, 34, 39, 43, 45, 65]. Shales also tend to be very fissile in that they fracture along a smooth surface aligned with the bedding plane [5, 25, 26, 34, 45]. Fissility is a shale property that further promotes anisotropy, particularly with respect to fluid flow [19, 72]. Stress-induced anisotropy, in which bedding-parallel microcracks induce significant differences in strength and stiffness depending on the directions of the principal stresses, has been noted by numerous investigators [22, 36, 46, 66].

Laboratory experiments on different types of shale reveal that this rock also exhibits pronounced viscous creep behavior under isotropic compression and/or triaxial stress conditions [20, 31, 55, 56, 58, 67]. Sone and Zoback [58] carried out a series of triaxial laboratory tests to study the elastic moduli, ductile creep behavior, and brittle strength of shale-gas reservoir rocks. They found that viscoplastic creep strain is linear with the applied differential stress and has a strong correlation with the volume of clay plus kerogen. They also reported that the tendency to creep is well correlated with the static Young's modulus, and explained it by appealing to the stress partitioning that occurs between the softer components of shale (clay and kerogen) and the stiffer components (quartz, feldspar, pyrite, and carbonates). In addition, the reduction in sample volume during creep suggested that creep was accommodated by pore compaction [6, 7].

Creep in shale is an important factor in the assessment of land subsidence [21] and wellbore stability [33]. Shales that creep exhibit significant secondary consolidation whose magnitude may be compared to that induced by primary consolidation in soils [9, 16, 42, 71]. In hydraulic fracturing, shales that exhibit significant creep may be too viscous to stimulate by brittle fracturing, and thus promote proppant embedment to keep the fractures from closing [48]. In general, creep testing of shale is one of the most challenging laboratory problems in rock engineering due to the significance of load directions and slow pore pressure transients [28]. It is also made more complicated by the fact that shales are highly heterogeneous, and that creep deformations occur at multiple scales.

Very recently, the first author's research team [11, 23, 24] has attempted to explain creep as a manifestation of secondary compression in multiple-porosity media, in which fluids are expelled from micron- to submicron-scale pores at

much longer time scales than they are expelled from millimeter-size pores. Whereas such explanation is meaningful when fluids are present in the pores, it does not help explain why shale continues to creep even when fluids are not present in the pores. In this paper, we capture such inelastic viscous response using viscoplasticity in the context of critical state theory. This approach is more meaningful than the more commonly used viscoelasticity, given that creep deformation in shale is both viscous and inelastic. Further, to keep the model sufficiently simple but robust, we accommodate the effect of heterogeneity in composition by considering shale as a mixture of softer matter and harder matter and obtain the overall constitutive response through volume averaging. We then use this critical state model to interpret and capture the results of multiscale laboratory creep tests in organic-rich shale.

2 Theory

We consider a heterogeneous solid consisting of a mixture of two materials M and m occupying approximately the same fraction of the total volume. We assume that these materials form their own solid skeleton so that they could each generate intrinsic stresses within them. We note at the outset that the problem is different from that considered by Hill [32], in which two solid phases are assumed to be firmly bonded together such that one phase can be regarded as inclusions in a matrix of the other. In our formulation, there are no inclusions and no dominant matrix—both solid phases form continuous solid frames whose displacement fields are also continuous.

2.1 General framework

Let $\boldsymbol{\sigma}_M$ denote the intrinsic Cauchy stress tensor in material M, and $\boldsymbol{\sigma}_m$ the intrinsic Cauchy stress tensor in material m. Denoting the volume fractions as ϕ^M and ϕ^m such that $\phi^M + \phi^m = 1$, the corresponding partial stress tensors are

$$\boldsymbol{\sigma}^M = \phi^M \boldsymbol{\sigma}_M \,, \qquad \boldsymbol{\sigma}^m = \phi^m \boldsymbol{\sigma}_m \,. \tag{1}$$

The total Cauchy stress tensor acting on the mixture takes the usual form

$$\boldsymbol{\sigma} = \boldsymbol{\sigma}^M + \boldsymbol{\sigma}^m \,, \tag{2}$$

or, in rate form (assuming infinitesimal theory so that the volume fractions remain essentially constant),

$$\dot{\boldsymbol{\sigma}} = \phi^M \dot{\boldsymbol{\sigma}}_M + \phi^m \dot{\boldsymbol{\sigma}}_m = \sum_{\alpha=M,m} \phi^\alpha \dot{\boldsymbol{\sigma}}_\alpha \,. \tag{3}$$

From physical consideration, we assume that there is no relative motion between the two materials in the sense that the organics and clay (material

m), for example, do not squeeze out of the harder rock matrix (material M). Since both phases are continuous and their displacement fields are also continuous, the strains must be uniform and $\boldsymbol{\epsilon}_M = \boldsymbol{\epsilon}_m \equiv \boldsymbol{\epsilon}$. In the context of viscoplasticity, the rate-constitutive equation for each of the two materials then takes the form

$$\dot{\boldsymbol{\sigma}}_\alpha = \boldsymbol{c}^e_\alpha : \left(\dot{\boldsymbol{\epsilon}} - \dot{\boldsymbol{\epsilon}}^{vp}_\alpha\right), \qquad \alpha = M, m, \tag{4}$$

where $\boldsymbol{c}^e_\alpha$ and $\dot{\boldsymbol{\epsilon}}^{vp}_\alpha$ are, respectively, the tangential elasticity tensor and viscoplastic strain rate for material α. Substituting into (3) and re-arranging yields the following expression for the total Cauchy stress tensor:

$$\dot{\boldsymbol{\sigma}} = \boldsymbol{c}^e : \left(\dot{\boldsymbol{\epsilon}} - \dot{\boldsymbol{\epsilon}}^{vp}\right), \tag{5}$$

where

$$\boldsymbol{c}^e = \sum_{\alpha=M,m} \phi^\alpha \boldsymbol{c}^e_\alpha \tag{6}$$

is the overall tangential elasticity tensor for the mixture, and

$$\dot{\boldsymbol{\epsilon}}^{vp} = \boldsymbol{c}^{e-1} : \Big(\sum_{\alpha=M,m} \phi^\alpha \boldsymbol{c}^e_\alpha : \dot{\boldsymbol{\epsilon}}^{vp}_\alpha \Big) \tag{7}$$

is the overall viscoplastic strain rate for the heterogeneous solid. Note that $\dot{\boldsymbol{\epsilon}}^{vp}$ is the weighted sum of $\dot{\boldsymbol{\epsilon}}^{vp}_M$ and $\dot{\boldsymbol{\epsilon}}^{vp}_m$; the weights are $\phi^M(\boldsymbol{c}^{e-1} : \boldsymbol{c}^e_M)$ and $\phi^m(\boldsymbol{c}^{e-1} : \boldsymbol{c}^e_m)$, which reduce to the volume fractions when $\boldsymbol{c}^e_M = \boldsymbol{c}^e_m \equiv \boldsymbol{c}^e$.

Remark. For the problem of inclusions, Hill [32] noted that the assumption of uniform strain is equivalent to the Reuss and Voigt estimates and is incorrect, since the Reuss estimate would imply that the inclusions and matrix could not remain bonded while the Voigt stresses would produce tractions at the interfaces that are not in equilibrium. However, as noted earlier, the present problem is not the same as that of inclusions. If the two phases were allowed to experience unequal strains, then the two displacement fields would be distinct and there would be relative motion between the two phases, which is physically unacceptable in the present setting. In contrast, one should note that the displacement fields characterizing the motion of the inclusions are inherently discontinuous. In addition, because each phase could generate interface forces against the other (unlike inclusions which cannot generate such interface forces because they are discontinuous), equilibrium at the interfaces would not be an issue. One should note that such interface forces naturally arise between phases in the context of mixture theory.

2.2 Rate-independent elastoplasticity

Consider two yield functions $f_M(\boldsymbol{\sigma}_M, p_{cM})$ and $f_m(\boldsymbol{\sigma}_m, p_{cm})$, where p_{cM} and p_{cm} define stress-like plastic internal variables, often called preconsolidation

stresses, for the two materials. Under an overall strain rate tensor $\dot{\boldsymbol{\epsilon}}$, we first consider the inviscid elastoplastic limit where $f_\alpha = \dot{f}_\alpha = 0$ for $\alpha = M, m$. Adopting the associative flow rule for the plastic flow direction yields the following expressions for the plastic multipliers [12]

$$\dot{\lambda}_\alpha = \frac{1}{\chi_\alpha} \frac{\partial f_\alpha}{\partial \boldsymbol{\sigma}_\alpha} : \boldsymbol{c}^e_\alpha : \dot{\boldsymbol{\epsilon}} \geq 0 \,, \tag{8}$$

where

$$\chi_\alpha = \frac{\partial f_\alpha}{\partial \boldsymbol{\sigma}_\alpha} : \boldsymbol{c}^e_\alpha : \frac{\partial f_\alpha}{\partial \boldsymbol{\sigma}_\alpha} + \mathcal{H}_\alpha > 0, \tag{9}$$

and $\mathcal{H}_\alpha$ is the plastic modulus.

In the elastoplastic limit, the rate constitutive equation takes the familiar form

$$\dot{\boldsymbol{\sigma}} = \boldsymbol{c}^{ep} : \dot{\boldsymbol{\epsilon}} \,, \tag{10}$$

where $\boldsymbol{c}^{ep}$ is the continuum elastoplastic tangential moduli tensor given by

$$\boldsymbol{c}^{ep} = \sum_{\alpha=M,m} \phi^\alpha \boldsymbol{c}^{ep}_\alpha \,, \tag{11}$$

and

$$\boldsymbol{c}^{ep}_\alpha = \boldsymbol{c}^e_\alpha - \frac{1}{\chi_\alpha} \boldsymbol{c}^e_\alpha : \frac{\partial f_\alpha}{\partial \boldsymbol{\sigma}_\alpha} \otimes \frac{\partial f_\alpha}{\partial \boldsymbol{\sigma}_\alpha} : \boldsymbol{c}^e_\alpha \,, \quad \alpha = M, m \,. \tag{12}$$

Note that the overall elastoplastic tangential moduli tensor is also the weighted average of the elastoplastic tangential moduli tensors for the two material components.

2.3 Rate-dependent viscoplasticity

We now consider the viscoplastic range. There are numerous possible forms for the viscoplastic strain rate [47, 49, 70, 75, 76], but here we employ two commonly used theories. The first of these is the form proposed by Duvaut and Lions [29],

$$\dot{\boldsymbol{\epsilon}}^{vp}_\alpha = \frac{1}{\tau_\alpha} \boldsymbol{c}^{e-1}_\alpha : (\boldsymbol{\sigma}_\alpha - \boldsymbol{\sigma}^\circ_\alpha) \,, \quad \alpha = M, m \,, \tag{13}$$

where $\boldsymbol{\sigma}^\circ_\alpha$ is the closest-point projection of $\boldsymbol{\sigma}_\alpha$ on the yield surface $f_\alpha = 0$, and τ_α is the relaxation time. The closest point projection is the position of the stress point if the over-stress $\boldsymbol{\sigma}_\alpha$ is mapped back to the yield surface in a rate-independent manner. The second form of the viscoplastic strain rate is due to Perzyna [44],

$$\dot{\boldsymbol{\epsilon}}^{vp}_\alpha = \frac{\langle f_\alpha \rangle}{\eta_\alpha} \frac{\partial f_\alpha}{\partial \boldsymbol{\sigma}_\alpha} \,, \quad \alpha = M, m, \tag{14}$$

where $\langle\cdot\rangle$ are the Macauley brackets, and η_α is a viscosity coefficient. Both forms for the viscoplastic strain rate are developed further in what follows.

In contrast to classical theory of plasticity, no consistency condition is imposed in viscoplasticity theory since the yield function is not required to satisfy any constraint. However, with viscoplasticity it is also necessary to perform a time-integration of the rate-dependent constitutive relations. Consider the Duvaut-Lions form for the viscoplastic strain rate, for example. Substituting (13) into (4) yields the rate equation

$$\dot{\boldsymbol{\sigma}}_\alpha = \boldsymbol{c}^e_\alpha : \dot{\boldsymbol{\epsilon}} - \frac{1}{\tau_\alpha}(\boldsymbol{\sigma}_\alpha - \boldsymbol{\sigma}^\circ_\alpha)\,, \quad \alpha = M, m\,. \tag{15}$$

A simple backward implicit time-integration over time interval Δt yields

$$\boldsymbol{\sigma}_{\alpha,n+1} = \frac{\boldsymbol{\sigma}^{\rm tr}_{\alpha,n+1} + (\Delta t/\tau_\alpha)\boldsymbol{\sigma}^\circ_{\alpha,n+1}}{1 + \Delta t/\tau_\alpha}\,, \tag{16}$$

where

$$\boldsymbol{\sigma}^{\rm tr}_{\alpha,n+1} = \boldsymbol{\sigma}_{\alpha,n} + \boldsymbol{c}^e_\alpha : \Delta\boldsymbol{\epsilon} \tag{17}$$

is the elastic stress predictor. We recall that the backward implicit scheme is only first-order accurate; however, it is unconditionally stable, which is a desirable feature of the algorithm since it allows for the use of a very large time step without concern that the solution will blow up. As a check, we see that the elastic stress predictor is recovered when $\Delta t/\tau_\alpha \to 0$ (i.e., $\boldsymbol{\sigma}_{\alpha,n+1} \to \boldsymbol{\sigma}^{\rm tr}_{\alpha,n+1}$), and that the rate-independent elastoplastic limit is obtained when $\Delta t \to \infty$ (i.e., $\boldsymbol{\sigma}_{\alpha,n+1} \to \boldsymbol{\sigma}^\circ_\alpha$).

Next, we consider the Perzyna model (see [37] for its predictive potential for modeling granular material behavior) for which the rate constitutive equation takes the form

$$\dot{\boldsymbol{\sigma}}_\alpha = \boldsymbol{c}^e_\alpha : \dot{\boldsymbol{\epsilon}} - \boldsymbol{c}^e_\alpha : \frac{\langle f_\alpha\rangle}{\eta_\alpha}\frac{\partial f_\alpha}{\partial \boldsymbol{\sigma}_\alpha}\,, \quad \alpha = M, m\,. \tag{18}$$

Assuming $f_\alpha > 0$, we can remove the Macauley brackets and employ a simple backward implicit time integration once again to obtain

$$\boldsymbol{\sigma}_{\alpha,n+1} = \boldsymbol{\sigma}^{\rm tr}_{\alpha,n+1} - \frac{\Delta t}{\eta_\alpha}\,\boldsymbol{c}^e_\alpha : \left(f_\alpha \frac{\partial f_\alpha}{\partial \boldsymbol{\sigma}_\alpha}\right)_{n+1}\,, \tag{19}$$

where the quantities inside the symbol $(\cdot)_{n+1}$ are evaluated at the unknown stress configuration $\boldsymbol{\sigma}_{\alpha,n+1}$. The Perzyna model generally requires an iterative solution of simultaneous nonlinear equations for the unknown stress configuration $\boldsymbol{\sigma}_{\alpha,n+1}$. The technique is developed further in the next section in the context of anisotropic and isotropic critical state models.

After the stress configurations $\boldsymbol{\sigma}_{\alpha,n+1}$ have been determined for $\alpha = M$ and m, the overall Cauchy stress tensor can be calculated from the weighted average

$$\boldsymbol{\sigma}_{n+1} = \sum_{\alpha=M,m} \phi^{\alpha} \boldsymbol{\sigma}_{\alpha,n+1} \,. \tag{20}$$

Remark. It is obvious from (14) that the unit for the viscosity coefficient η depends on the unit for the yield function f. If f has a unit of F/L^2 (stress), then η has a unit of FT/L^2 (e.g., Pa $\cdot$ s). If f has a unit of F^2/L^4 (stress squared), then η has a unit of F^3T/L^6 (e.g., Pa$^3 \cdot$s). Since there is no unique way by which one can write the yield function f (for example, it can be written as a homogenous function of any degree n of the stress variable), there is no unique unit for the viscosity coefficient η.

2.4 Critical state models

We now present specific critical-state models that we propose to use for shale. For this material, the stiffer rock matrix may exhibit transverse isotropy in the mechanical response due to the existence of bedding planes, whereas the softer organics and clays embedded within the rock matrix may exhibit an isotropic behavior due to relatively random orientation of micron- and submicron-scale particles.

For material M, which exhibits transverse isotropy, we assume a rotated ellipsoidal yield function of the form

$$f_M(\boldsymbol{\sigma}^*, p_{cM}) = \frac{q^{*2}}{M_M^2} + p^*(p^* - p_{cM}) \,, \tag{21}$$

where $p^* = \mathrm{tr}(\boldsymbol{\sigma}^*)/3$, $q^* = \sqrt{3/2}\|\boldsymbol{s}^*\|$, $\boldsymbol{s}^* = \boldsymbol{\sigma}^* - p^*\mathbf{1}$, M_M is the slope of the critical state line, and p_{cM} is a stress-like plastic internal variable associated with material M. The stress tensor $\boldsymbol{\sigma}^*$ is a fictitious stress obtained from a linear map with respect to the real stress $\boldsymbol{\sigma}_M$ according to the equation

$$\boldsymbol{\sigma}^* = \mathbb{P} : \boldsymbol{\sigma}_M \,, \tag{22}$$

where $\mathbb{P}$ is a rotation operator given by

$$\begin{aligned} \mathbb{P} = c_1\mathbb{I} + \frac{c_2}{2}\big(\boldsymbol{m}\oplus\boldsymbol{m} + \boldsymbol{m}\ominus\boldsymbol{m}\big) \\ + \frac{c_3}{4}\big(\mathbf{1}\oplus\boldsymbol{m} + \boldsymbol{m}\oplus\mathbf{1} + \mathbf{1}\ominus\boldsymbol{m} + \boldsymbol{m}\ominus\mathbf{1}\big) \,, \end{aligned} \tag{23}$$

c_1, c_2, and c_3 are the anisotropy parameters, $\mathbf{1}$ is the second-order identity tensor (Kronecker delta), and $\mathbb{I}$ is the rank-four symmetric identity tensor. In the above expression for $\mathbb{P}$, $\boldsymbol{m}$ is the second-order microstructure tensor that defines the bedding plane orientation,

$$\boldsymbol{m} = \boldsymbol{n}\otimes\boldsymbol{n} \,, \tag{24}$$

where $\boldsymbol{n}$ is the unit normal to the bedding plane. The tensorial operators $\otimes$, $\oplus$, and $\ominus$ are defined such that $(\bullet\otimes\circ)_{ijkl} = (\bullet)_{ij}(\circ)_{kl}$, $(\bullet\oplus\circ)_{ijkl} = (\bullet)_{jl}(\circ)_{ik}$, and

$(\bullet \ominus \circ)_{ijkl} = (\bullet)_{il}(\circ)_{jk}$, see [52, 74, 75] for further details. Alternative tensorial forms of the constitutive equation are presented by Boehler and Sawczuk [10].

There has been some work done suggesting that the creep rate in source rocks is driven by isotropic constituents such as pores and organic matter, and that this creep rate is almost isotropic [54]. Thus, for material m we take the same modified Cam-Clay yield function but express it in isotropic form with respect to real stress $\boldsymbol{\sigma}_m$, i.e.,

$$f_m(\boldsymbol{\sigma}_m, p_{cm}) = \frac{q^2}{M_m^2} + p(p - p_{cm})\,, \tag{25}$$

where $p = \mathrm{tr}(\boldsymbol{\sigma}_m)/3$, $q = \sqrt{3/2}\|\boldsymbol{s}\|$, $\boldsymbol{s} = \boldsymbol{\sigma}_m - p\mathbf{1}$, M_m is the slope of the critical state line, and p_{cm} is a stress-like internal plastic variable associated with material m. In the viscoplastic range, an over-stress may be allowed in which the values of the yield functions f_M and f_m may be greater than zero.

Hardening and softening responses in critical state theory are generally governed by the volumetric component of the viscoplastic strain. Furthermore, we can incorporate thermal effects into the formulation through the preconsolidation stress $p_{c\alpha}$ according to the expression

$$\dot{p}_{c\alpha} = p_{c\alpha}\Big[\frac{\mathrm{tr}(\dot{\boldsymbol{\epsilon}}_\alpha^{vp})}{\lambda_\alpha^p} + \mathcal{G}(\Theta)\dot{\Theta}\Big]\,, \quad \alpha = M, m\,, \tag{26}$$

where λ_α^p is a plastic compressibility index and $\mathcal{G}$ is some function of absolute temperature Θ (assumed to be the same for materials M and m). Denoting the volumetric part of the viscoplastic strain rate by $\dot{\theta}_\alpha^{vp} = \mathrm{tr}(\dot{\boldsymbol{\epsilon}}_\alpha^{vp})$, and integrating the preconsolidation stress over time (t_n, t_{n+1}), yields the evolution equation

$$p_{c\alpha} = p_{c\alpha,n}\exp\Big(\frac{\theta_\alpha^{vp} - \theta_{\alpha,n}^{vp}}{\lambda_\alpha^p}\Big)\mathcal{F}(\Theta)\,, \quad \alpha = M, m\,, \tag{27}$$

where $p_{c\alpha,n}$ is the value of $p_{c\alpha}$ at time t_n, and $\mathcal{F}(\Theta) = \exp\big(\int_{t_n}^{t_{n+1}} \mathcal{G}(\Theta)\mathrm{d}\Theta\big)$. An example of this softening function is the Laloui and Cekerevac [35] softening law

$$\mathcal{F}(\Theta) = \Big[1 - \gamma_T \ln\Big(1 + \frac{\Delta\Theta}{\Theta_0 - 273}\Big)\Big]\,, \tag{28}$$

where γ_T is a thermal softening parameter. Other thermal softening laws are available in the literature, see [52].

2.5 Duvaut-Lions viscoplasticity

We now develop the Duvaut-Lions viscoplastic model within the framework of critical state theory. The volumetric component of the viscoplastic strain rate can be obtained by taking the trace of both the left- and right-hand sides of (13) as

$$\dot{\theta}^{vp}_{\alpha} = \frac{1}{\tau_\alpha}(\theta^{e}_{\alpha} - \theta^{e\circ}_{\alpha}) \equiv -\frac{1}{\tau_\alpha}(\theta^{vp}_{\alpha} - \theta^{\circ}_{\alpha})\,, \quad \alpha = M, m, \tag{29}$$

where $\theta^{e}_{\alpha} = \mathrm{tr}(\boldsymbol{c}^{e-1}_{\alpha} : \boldsymbol{\sigma}_\alpha) = \mathrm{tr}(\boldsymbol{\epsilon}^{e}_{\alpha})$, etc., and θ°_{α} is the inelastic volumetric strain at the closest-point-projection state. We note that $\theta^{e}_{\alpha} = \theta - \theta^{vp}_{\alpha}$ and $\theta^{e\circ}_{\alpha} = \theta - \theta^{\circ}_{\alpha}$, where $\theta = \theta_M = \theta_m$ from the assumption that the total strains in the two materials are the same. Equation (29) is a first-order ordinary differential equation in θ^{vp}_{α}, which can once again be integrated using the first-order accurate, unconditionally stable backward implicit scheme:

$$\theta^{vp}_{\alpha,n+1} = \frac{\theta^{vp}_{\alpha,n} + (\Delta t/\tau_\alpha)\theta^{\circ}_{\alpha,n+1}}{1 + \Delta t/\tau_\alpha}\,. \tag{30}$$

Substituting this last equation into (27) gives the integrated evolution equation for the preconsolidation stress,

$$p_{c\alpha} = p_{0\alpha}\exp\Big[\frac{1}{\lambda^{p}_{\alpha}} \cdot \frac{(\Delta t/\tau_\alpha)(\theta^{\circ}_{\alpha,n+1} - \theta^{vp}_{\alpha,n})}{1 + \Delta t/\tau_\alpha}\Big]\mathcal{F}(\Theta)\,, \quad \alpha = M, m\,. \tag{31}$$

Box 1 shows a summary of the algorithm. The step-by-step procedure is executed for $\alpha = M$, and then is repeated for $\alpha = m$. At the conclusion of the calculations, the overall total stress $\boldsymbol{\sigma}_{n+1}$ is obtained from (20). Note the sequential calculations involving closest-point projection for rate-independent elastoplasticity (Step 3), followed by an update of the variables for rate-dependent viscoplasticity (Step 4). This sequence of calculations facilitates ease in coding since one can simply skip Step 4 if the rate-independent option of the model is desired.

For $\alpha = M$ and m:

Step 1. Compute $\boldsymbol{\sigma}^{\mathrm{tr}}_{\alpha,n+1} = \boldsymbol{\sigma}_{\alpha,n} + \boldsymbol{c}^{\mathrm{e}}_{\alpha} : \Delta\boldsymbol{\epsilon}$ and $p_{c\alpha,n+1} = p_{c\alpha,n}$.
Step 2. Check $f_\alpha < 0$?
Yes, elastic response: Set $\boldsymbol{\sigma}_{\alpha,n+1} = \boldsymbol{\sigma}^{\mathrm{tr}}_{\alpha,n+1}$ and exit.
Step 3. No, viscoplastic response:
Compute $\boldsymbol{\sigma}^{\circ}_{\alpha}$ and θ°_{α} from closest-point projection.
Step 4. Compute $\boldsymbol{\sigma}_{\alpha,n+1}$ from (16) and $p_{c\alpha,n+1}$ from (31) and exit.

Box 1. Algorithm for critical state viscoplasticity, Duvaut-Lions version.

In conventional nonlinear finite element analysis, an algorithmic stress-strain tensor is necessary to construct the global tangent operator. To this end, we differentiate (20) with respect to the applied strain to obtain

$$\boldsymbol{c}_{n+1} := \frac{\partial \boldsymbol{\sigma}_{n+1}}{\partial \boldsymbol{\epsilon}_{n+1}} = \sum_{\alpha=M,m} \phi^\alpha \frac{\partial \boldsymbol{\sigma}_{\alpha,n+1}}{\partial \boldsymbol{\epsilon}_{n+1}}$$
$$= \sum_{\alpha=M,m} \phi^\alpha \Big[\frac{\boldsymbol{c}^e_\alpha + (\Delta t/\tau_\alpha)\boldsymbol{c}^\circ_{\alpha,n+1}}{1+\Delta t/\tau_\alpha} \Big], \tag{32}$$

where $\boldsymbol{c}^\circ_{\alpha,n+1}$ is the algorithmic stress-strain moduli tensor consistent with the closest-point projection algorithm for rate-independent elastoplasticity. Once again, this result facilitates ease in coding since the same algorithm can be used for both rate-independent and rate-dependent options. Semnani et al. [52] and Zhao et al. [74] present the mathematical expression for the tangent operator $\boldsymbol{c}^\circ_{\alpha,n+1}$.

2.6 Perzyna viscoplasticity

We next develop the Perzyna viscoplastic version of the critical state theory. To this end, we first consider the general anisotropic case for which the yield function cannot be expressed in terms of stress invariants and where the stress-point integration algorithm is given by (19). Symbolically, for the anisotropic case the yield function may be expressed in the general form $f_\alpha = f_\alpha(\boldsymbol{\sigma}_\alpha, p_{c\alpha})$, where $p_{c\alpha}$ is obtained from the implicit integration

$$p_{c\alpha,n+1} = p_{c\alpha,n} \exp\Big[\frac{\Delta t}{\lambda^p_\alpha} \frac{f_{\alpha,n+1}}{\eta_\alpha} \mathrm{tr}\Big(\frac{\partial f_\alpha}{\partial \boldsymbol{\sigma}_\alpha} \Big)_{n+1} \Big] \mathcal{F}(\Theta)\,, \quad \alpha = M, m\,. \tag{33}$$

For a given temperature Θ, one can solve (19) and (33) simultaneously for $\boldsymbol{\sigma}_{\alpha,n+1}$ and $p_{c\alpha,n+1}$, resulting in a total of seven unknowns for 3D problems.

Appendix A shows the procedure for integrating the Perzyna viscoplastic model. The algorithm resembles the integration for rate-independent critical state plasticity except that the plastic multiplier is replaced by the analytically known function $\langle f \rangle/\eta$. This, in a way, makes the viscoplastic formulation easier to handle because there is no constraint on the sign of the yield function. Included in Appendix A is the derivation of the algorithmic stress-strain moduli tensor for the Perzyna model. Box 2 shows the step-by-step calculations for the Perzyna model.

For $\alpha = M$ and m:

Step 1. Compute $\boldsymbol{\sigma}^{\mathrm{tr}}_{\alpha,n+1} = \boldsymbol{\sigma}_{\alpha,n} + \boldsymbol{c}^{\mathrm{e}}_\alpha : \Delta\boldsymbol{\epsilon}$ and $p_{c\alpha,n+1} = p_{c\alpha,n}$.
Step 2. Check $f_\alpha < 0$?
Yes, elastic response: Set $\boldsymbol{\sigma}_{\alpha,n+1} = \boldsymbol{\sigma}^{\mathrm{tr}}_{\alpha,n+1}$ and exit.
Step 3. No, viscoplastic response:
Compute $\boldsymbol{\sigma}_{\alpha,n+1}$ from (19) and $p_{c\alpha,n+1}$ from (33) and exit.

Box 2. Algorithm for critical state viscoplasticity, Perzyna version.

For the special case of isotropic viscoplasticity (i.e., $\alpha = m$), the stress-point integration can be performed more conveniently in the stress invariant space, as illustrated below. For brevity in notations, we shall drop the subscripts for the present discussion and take $(\cdot) = (\cdot)_{m,n+1}$. Let K and μ denote the elastic bulk and shear moduli for the isotropic material, respectively. The relevant update equations assuming backward implicit time integration are as follows:

$$\left.\begin{aligned} p &= p^{\mathrm{tr}} - K\frac{\Delta t}{\eta}\Big(f\frac{\partial f}{\partial p}\Big) \\ q &= q^{\mathrm{tr}} - 3\mu\frac{\Delta t}{\eta}\Big(f\frac{\partial f}{\partial q}\Big) \\ p_c &= p_{c,n}\exp\Big[\frac{\Delta t}{\lambda^p\eta}\Big(f\frac{\partial f}{\partial p}\Big)\Big]\mathcal{F}(\Theta) \end{aligned}\right\}, \tag{34}$$

where $\partial f/\partial p = 2p - p_c$, $\partial f/\partial q = q/M^2$, and $f = f(p, q, p_c) > 0$ for the modified Cam-Clay yield function. The above three equations can be solved for p, q, and p_c, after which the Cauchy stress tensor can be constructed from the equation

$$\boldsymbol{\sigma} = p\mathbf{1} + \sqrt{\frac{2}{3}}q\hat{\boldsymbol{n}}\,, \tag{35}$$

where $\hat{\boldsymbol{n}} = \boldsymbol{s}/\|\boldsymbol{s}\|$, and $\boldsymbol{s} = \mathrm{dev}(\boldsymbol{\sigma})$. Appendix B shows the simplified version of the Perzyna theory for the case of an isotropic, two-invariant yield function.

Remark. As noted in [12], critical state models (and many practical constitutive models for that matter) generally do not follow the principle of maximum plastic dissipation [53], even if they obey the associative flow rule, because the hardening laws for these models are mostly empirical and not derived from any normality condition. Nevertheless, the discussions of this section demonstrate that there is no ambiguity on the evolution of all variables, and that the proposed constitutive formulation remains deterministic and complete.

3 Numerical simulations

In this section, we use numerical simulations to highlight important features of the viscoplastic Cam-Clay model. The first example involves a comparison of creep strains predicted by the Perzyna and Duvaut-Lions viscoplastic models at various bedding plane orientations assuming a single material description, i.e., no distinction is made between softer and harder materials. Next, we employ the two-material description to capture the creep strain responses of

anisotropic Barnett shale under triaxial stress condition. Then we demonstrate the impact of spatial heterogeneity in material composition on the overall creep of a rectangular specimen of shale. We emphasize that all material parameters used in the following examples were derived from the literature, thus ensuring that the calculated responses are realistic and representative of those encountered in the field.

3.1 Duvaut-Lions and Perzyna formulations compared

We first compare the creep responses predicted by the two viscoplastic models, focusing on the calibration of the relaxation time τ of the Duvaut-Lions model and viscosity coefficient η of the Perzyna model.

A transversely isotropic elastic material requires five elastic constants. For this example, we derive these constants for a shale belonging to the Westgate Formation of the Upper Cretaceous Colorado Group taken from an exploration well near Cold Lake, Alberta, Canada, as reported by Wong et al. [69]. The elastic parameters were measured from ultrasonic tests and include the Young's modulus along the bed-parallel (BP) direction E_h, Young's modulus along the bed-normal (BN) direction E_v, Poisson's ratio for stress applied and strain measured along the BP direction ν_{hh}, Poisson's ratio for stress applied in the BN and strain measured in the BP directions ν_{vh}, and the shear modulus along the BN direction G_{vh}. We convert them into the five elastic parameters adopted by Namani et al. [40] and Zhao et al. [74], which include the Lamé parameter λ, shear modulus along the BN direction μ_1, shear modulus along the BP direction μ_2, and the two anisotropy parameters α and β. The original and converted elastic parameters are summarized in Table 1.

Table 1. Elastic material parameters for shale, all in MPa except Poisson's ratios.

original	E_h	4741	converted	λ	60
	E_v	3991		μ_1	1820
	ν_{hh}	0.01		μ_2	2350
	ν_{vh}	0.05		α	150
	G_{vh}	1822		β	1070

The studies of Wong et al. [69] only focused on the elastic properties of the Cold Lake shale, and did not include the properties of this material in the inelastic regime. Here, we assume that the inelastic properties are similar to those of synthetic rocks tested by Tien et al. [61]. These artificial rocks were produced by mixing different weight ratios of kaolinite, cement, and water, and layering them alternately to create artificial transversely isotropic rocks. The inelastic properties of these rocks were then inferred by Zhao et al. [74] from the experiments conducted at a confining pressure of 6 MPa. The parameters consist of the slope of the critical state line M, compressibility parameter λ^p,

and the three anisotropy parameters, c_1, c_2 and c_3, which are all summarized in Table 2.

Table 2. Calibrated Cam-Clay parameters from tests on a synthetic rock at a confining pressure of 6 MPa.

M	λ_p	c_1	c_2	c_3
2.0	0.0026	0.82	−0.33	0.36

Using the aforementioned parameters, we now simulate the drained creep response of the shale using the following loading protocol. First, we assume the shale to be normally consolidated and apply an all-around confining pressure of 6 MPa on a triaxial sample of this material. The axial stress is then increased instantaneously to 7.5 MPa while the radial stress is maintained at 6 MPa, resulting in a stress difference of 1.5 MPa. The material is then allowed to creep under this sustained state of stress.

Figure 1 shows the time-variation of the axial creep strain at a sustained stress difference of 1.5 MPa assuming a horizontal bedding plane (i.e., $\theta = 0$). Note from this figure that when the stress difference is relatively small compared with p_c, the ratio η/τ can be adjusted so that the creep strain responses calculated by the Perzyna and Duvaut-Lions models are nearly the same. Unlike the Duvaut-Lions formulation, which calculates the inviscid response at each time step, the Perzyna formulation cannot determine the inviscid solution in one time step since setting $\eta = 0$ will result in a singular solution. However, when the inviscid solution is difficult to calculate, such as in contact problem and other stiff systems, the Perzyna formulation can be used for viscoplastic regularization. Regardless of the model, higher values of η or τ lead to slower creep strain rates, and when these two parameters approach infinity, one readily recovers the elastic solution.

Figures 2 and 3 depict an interesting trend when the cumulative axial creep strains are plotted versus bedding plane orientation θ. Note that for this hypothetical shale, the axial creep strains are higher when the axial load is applied in the weaker BN direction ($\theta = 0$) than when it is applied in the stronger BP direction ($\theta = 90°$). Also note the asymmetric hump that the cumulative axial strains exhibit at different time instants when plotted with respect to bedding plane orientation θ (see Fig. 3). This feature resembles an inverted U-shaped curve with shoulders that characterizes the variation of strength with bedding plane orientation [74]. For this particular shale, the cumulative axial creep strain is thus larger when the load is applied at an angle to the bedding plane than when it is applied in either BN or BP directions.

Figure 4 shows the convergence profiles of Newton-Raphson iteration and suggests that all iterations converged to machine precision. Creep is a stress-controlled process, so these convergence profiles reflect the properties of the algorithmic tangent operator that may be employed for boundary-value prob-

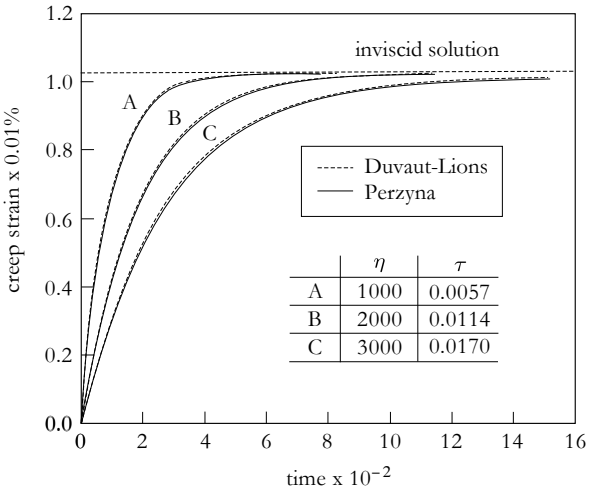

	η	τ
A	1000	0.0057
B	2000	0.0114
C	3000	0.0170

Fig. 1. Axial creep strains in the BN direction for viscosity-relaxation time ratio of $\eta/\tau = 1.75 \times 10^5$ MPa^3. Units: η is in MPa^3· h; τ and time are in h.

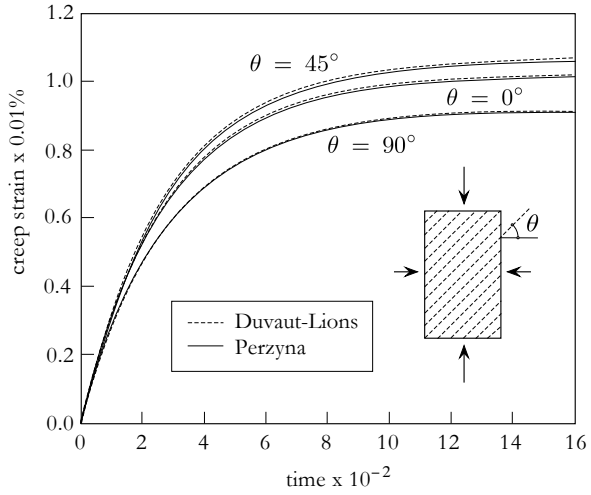

Fig. 2. Creep strain as a function of bedding plane orientation θ for viscosity $\eta =$ 3000 MPa^3· h and relaxation time $\tau = 0.017$ h.

lem simulations. We should note that all calculations were done in 32-bit precision and satisfied a very stringent convergence criterion.

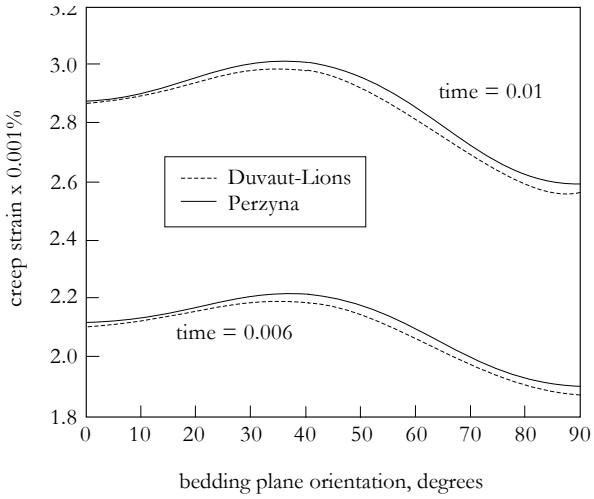

Fig. 3. Axial creep strain versus bedding plane orientation θ showing an asymmetric hump. Viscosity $\eta = 3000$ MPa$^3\cdot$ h, relaxation time $\tau = 0.017$ h; time is in h.

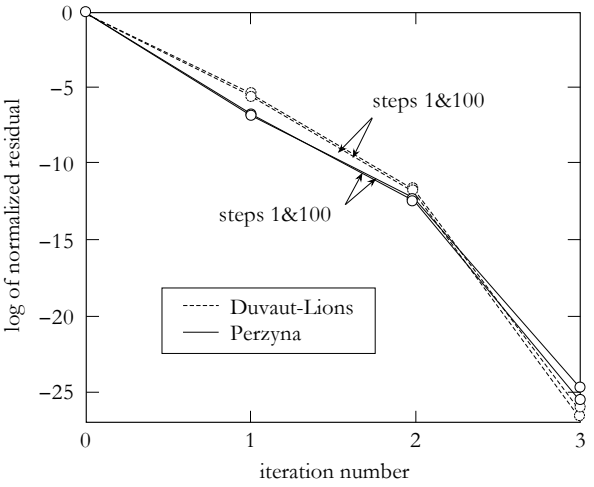

Fig. 4. Convergence profiles of Newton-Raphson iterations for Duvaut-Lions and Perzyna viscoplastic models.

Remark. More elaborate forms for the viscoplastic function are available for both Duvaut-Lions and Perzyna models, see References [50, 53]. For example, for Duvaut-Lions model, one can insert a function of the form $g(E)/\tau_\alpha$ in lieu of $1/\tau\alpha$ in equation (13), where E is some energy norm; and for Perzyna model, one can use a nonlinear function of $\langle f_\alpha \rangle$ in equation (14). However,

the next section shows the linear forms to be sufficient for capturing the creep responses of a shale, and will thus be pursued from here on.

3.2 Creep of Barnett shale

Sone and Zoback [57, 58] conducted triaxial creep tests on a shale-gas reservoir rock called Barnett shale. This sedimentary rock is a typical geological formation located in the Bend Arch-Fort Worth Basin in Texas, USA. Tests were conducted on cylindrical samples of 25.4 mm diameter and 30.5–53.3 mm length, with the axial load applied either in BN ($\theta = 0$) or BP ($\theta = 90°$) directions. On average, shale samples tested consisted of 52% QFP (quartz, feldspar and pyrite) and 48% clay and kerogen by volume. Thus, a two-material description is appropriate for simulating these tests. Here, we model the harder QFP matrix with a transversely isotropic solid frame, and the softer clay-kerogen component with an isotropic solid frame. With this separation, shale anisotropy is incorporated into the harder solid matrix, whereas ductile creep behavior is mostly attributed to the softer matrix.

Sone and Zoback [57, 58] only provided creep and strength response data but not the elastic and plastic mechanical properties of this shale, so we have to make some assumptions. Since the present work focuses mainly on creep, we herein assume the following material parameters for this shale. For the elastic parameters, the five constants of the transversely isotropic harder frame [40] and the two constants of the isotropic softer frame are summarized in Table 3. The elastic properties for the harder frame are similar to those of pure quartz [4], which is strictly not transversely isotropic but belongs to trigonal crystal group characterized by six elastic constants. To obtain transverse isotropy, we simply ignore the non-zero entries that are not consistent with the elastic moduli operator for a transversely isotropic material. As an aside, we note that for Barnett shale the S-wave modulus in BP direction is reported to be higher than in BN direction [57]; this feature is reflected in the values of μ_h displayed in Table 3. As for the softer frame, the stiffness of clay and kerogen generally varies widely with water content; for the present study, they are chosen to be comparable to the elastic properties of clay as reported by Bayuk et al. [3].

Table 3. Assumed elastic material parameters for Barnett shale, all in MPa.

harder frame	λ_h	7400	softer frame	λ_s	6700
	μ_{h1}	58000		μ_{s1}	1700
	μ_{h2}	63000		μ_{s2}	1700
	α_h	4500		α_s	–
	β_h	−65000		β_s	–

The assumed Cam-Clay parameters for the harder and softer frames are displayed in Table 4. The slope of the critical state line M was estimated from

a friction angle of $\phi_{cs} \approx 40^\circ$ reported by Sone and Zoback [58] from strength tests conducted subsequent to creep, along with the standard formula relating M with ϕ_{cs} given in Reference [12]. For the harder frame, the remaining parameters are comparable to those used by Semnani et al. [52] and Zhao et al. [74] that were mostly inferred from Tournemire shale data [41]. For the softer frame, the compressibility index is assumed to be 20 times higher. More realistic values of these parameters may be inferred from conducting small-scale tests that can probe the properties of the shale constituents, such as the nano- and/or micro-indentation tests [8], although this is beyond the scope of the present paper.

Table 4. Cam-Clay parameters for Barnett shale.

harder frame	M_h	1.6	softer frame	M_s	1.6
	λ_{hp}	0.00013		λ_{sp}	0.0026
	c_{h1}	0.73		c_{s1}	1.0
	c_{h2}	-0.20		c_{s2}	$-$
	c_{h3}	0.40		c_{s3}	$-$

The loading protocol follows the experimental procedure described in Reference [58]. First, we prescribe an initial preconsolidation pressure of $p_{c0} = 35$ MPa, which equals the in-situ effective stress where the shale samples were taken. Then, we apply a hydrostatic pressure of 20 MPa followed by a stress difference of 48 MPa by increasing the axial stress while holding the radial stress fixed. The creep parameters have been selected to obtain a good fit with the laboratory creep data presented by Sone and Zoback [58], and are summarized below: $\eta_s = 1.3{\times}10^9$ MPa$^3{\cdot}$s; $\tau_s = 1$ s; and $\eta_h/\eta_s = \tau_h/\tau_s = 1000$. The results are plotted in Figures 5, 6, and 7 for the case where $\theta = 90^\circ$. Note that the horizontal axis in Fig. 5 is total time, whereas the horizontal axis in Figs. 6 and 7 is creep time. The instantaneous isotropic compression at $t = 0$ is represented by a Heaviside function in Fig. 5.

Figure 5 shows the total strains along the axial and two lateral (BN and BP) directions. During hydrostatic loading, the strain response is elastic and confirms the fact that the BP direction is stiffer than the BN direction for this shale sample [57]. After the axial stress is increased, both the axial and lateral strains change dramatically. Two stages of deformation can be identified: (a) nearly elastic stage where the load is increased fast enough that the viscoplastic deformation response is negligible; and (b) creep stage where the applied stress is held fixed and the yield surface expands in a rate-dependent manner to "catch up" with the fixed stress. During these two stages the sample compacts in the axial direction and dilates in the two (BN and BP) lateral directions, but the overall volume change is still characterized by compaction following what was observed during the experiments. Note that even during the creep stage the calculated lateral expansion in the BN direction remains

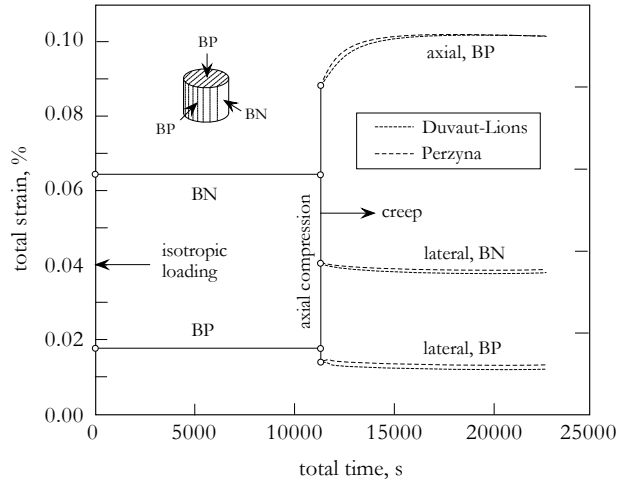

Fig. 5. Simulated total strains in Barnett shale sample before and during creep. Instantaneous isotropic compression at time $t = 0$ followed by instantaneous axial compression at time $t = 11000$ s result in elastic axial strain in BP direction and elastic lateral strains in BN and BP directions. Creep strains develop at $t > 11000$ s. Solid lines = elastic loading; dashed curves = creep.

greater than in the BP direction, although the experimental data did not make any distinction between the two lateral deformations.

We remark here that although the model has several parameters that can be calibrated, the process is not merely a matter of curve-fitting. In fact, no matter what values of parameters one chooses, the creep test results reported for this shale cannot be replicated by an isotropic viscoplastic formulation, or even by a transversely isotropic viscoplastic model that does not allow for inelastic volumetric compaction. Important elements must be represented for the model to capture the observed laboratory responses.

3.3 Strain localization at varying strain rates

We next present hypothetical numerical simulations of strain localization in a shale whose properties are similar to those reported in Section 3.2 for Barnett shale. Here, we go beyond the stress point calculations and conduct plane strain simulations of boundary-value problems.

The setup is shown in Fig. 8. We assume a rectangular sample having a width of 25.4 mm and a height of 50.8 mm, which is approximately the same size as the cylindrical shale sample tested by Sone and Zoback [58] under triaxial loading condition. The bedding plane orientation in the harder frame is assumed to be $\theta = 45^\circ$ with respect to the horizontal. The top and bottom ends are supported on rollers (i.e. smooth) except for the middle node

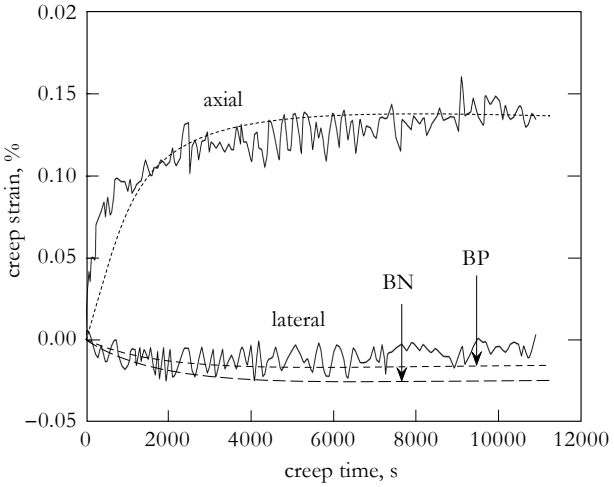

Fig. 6. Experimental (noisy data) and simulated (smooth curves) creep responses of Barnett shale sample, Duvaut-Lions viscoplasticity. Experimental data after Sone and Zoback [57, 58].

at the bottom end that is supported on a pin to arrest rigid-body horizontal translation. To trigger strain localization, the shale is assumed to be overconsolidated under a confining pressure of 1 MPa and a preconsolidation pressure of $p_{c0} = 35$ MPa. This ensures that the stress point resides on the dilative side of the yield surface, thus generating a softening response. We assume a homogeneous sample with 50% hard and 50% soft components by volume; a weak element with 30% hard and 70% soft is introduced at the center to initiate the shear band. The sample is then subjected to vertical compression at different strain rates.

We consider three vertical strain rates: $\dot{\epsilon}_A = 4 \times 10^{-6}$, $\dot{\epsilon}_B = 2 \times 10^{-7}$, and $\dot{\epsilon}_C = 2 \times 10^{-8}$, all in percent per second. To accommodate the changed loading condition (plane strain for this example versus axisymmetric for the previous example), we adjust the viscosity coefficients η_h and η_s of the Perzyna formulation to 1/30 of the values reported in Section 3.2, while keeping the same relaxation times τ_h and τ_s of the Duvaut-Lions formulation as in Section 3.2. This adjustment is not mandatory and is made solely for the purpose of generating nearly the same stress-strain responses, as shown in Figs. 9 and 10. Observe that strain rate $\dot{\epsilon}_A$ is too fast for the sample to produce a softening response. On the other hand, strain rates $\dot{\epsilon}_B$ and $\dot{\epsilon}_C$ are slow enough that the shale exhibits a softening response almost right at initial yield.

Deformed shapes and localized deformation patterns calculated using the Duvaut-Lions and Perzyna formulations are shown in Figs. 11 and 12, respec-

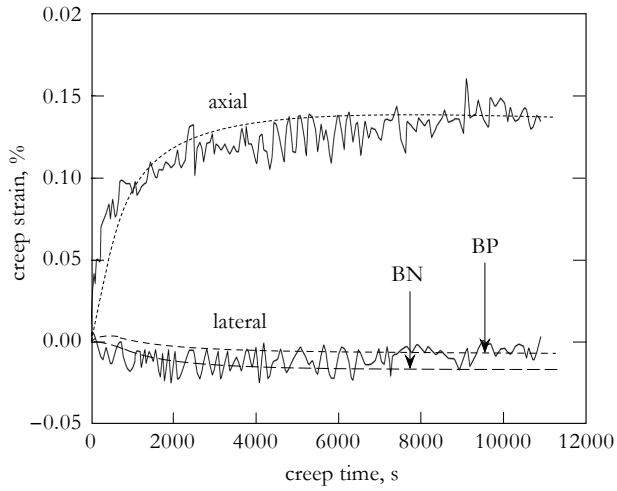

Fig. 7. Experimental (noisy data) and simulated (smooth curves) creep responses of Barnett shale sample, Perzyna viscoplasticity. Experimental data after Sone and Zoback [57, 58].

tively. Note that the shale domain swings to the right as it deforms, consistent with the weaker BN direction. Because of the significant elastic deformation occurring prior to strain localization, most of this swing may be attributed to elastic anisotropy. As noted earlier, the strain rate $\dot{\epsilon}_A$ is too fast for the shale to develop a softening response; thus, no deformation band is generated despite the presence of a weak element. On the other hand, the intermediate strain rate $\dot{\epsilon}_B$ results in a pair of conjugate deformation bands, although the band in the BN direction appears to be slightly more prominent. The slowest strain rate $\dot{\epsilon}_C$ generates a dominant deformation band in the BN direction. However, note that the band thickness increases with increasing deformation. This may be attributed in part to the dilative nature of the deformation band (it is a dilative shear band), which causes the localized zone to spread as the sample is compressed. We remark that viscoplasticity is a form of regularization that provides a characteristic length scale. Hence, in principle, no element enhancement is needed to accommodate the localized deformation produced in this example.

3.4 Creep-induced shear bands

In this example, we show through numerical simulations that creep deformation can also lead to strain localization. The process is different from simulations commonly seen in the literature in that the load here is constant while the shear bands are either emerging, spreading, and/or propagating. We present two sets of simulations: The first assumes a homogeneous shale

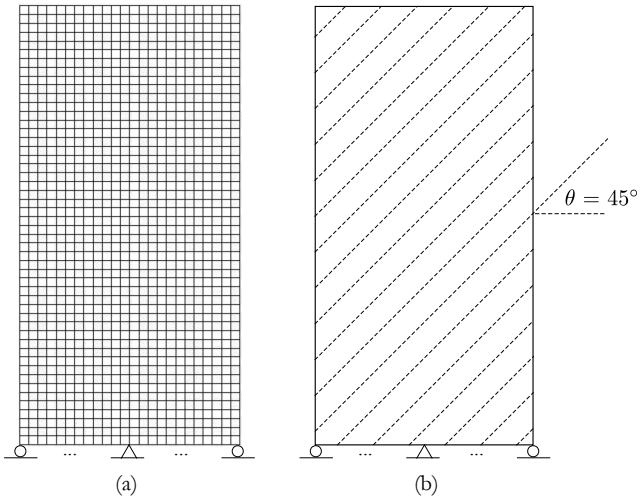

Fig. 8. Problem setup: (a) finite element mesh; (b) bedding plane orientation for harder material component.

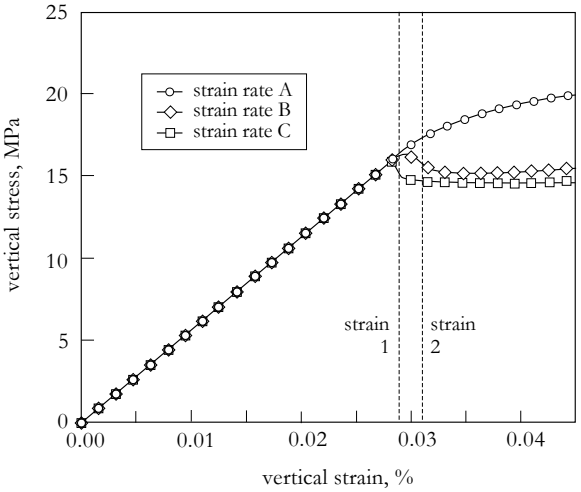

Fig. 9. Vertical stress versus vertical strain curves as functions of the vertical strain rate: Duvaut-Lions viscoplasticity.

sample with one weak element at the center, similar to the configuration of the previous section.The second considers a heterogeneous sample with spatially

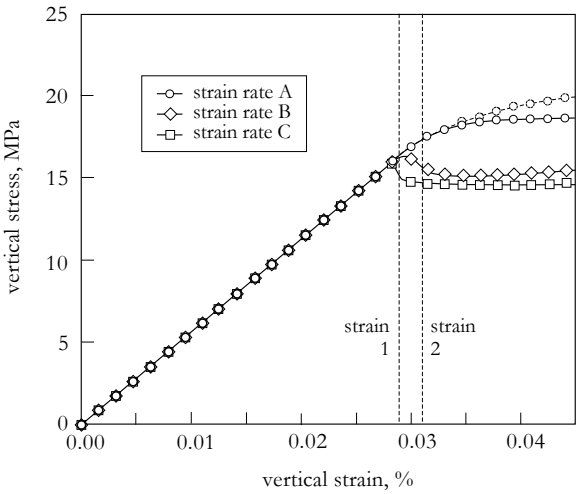

Fig. 10. Vertical stress versus vertical strain curves as functions of the vertical strain rate: Perzyna viscoplasticity. Dashed curve with dashed circular ticks is Duvaut-Lions curve at strain rate $\dot{\epsilon}_A$. For strain rates $\dot{\epsilon}_B$ and $\dot{\epsilon}_C$, the difference between the Duvaut-Lions and Perzyna curves is nearly imperceptible.

varying hard/soft volume fractions. The idea of introducing heterogeneity to trigger strain localization follows that adopted in References [2, 13, 14, 59, 60].

For the first set of simulations, Fig. 13 shows the evolution of the vertical displacement at the top of the sample after applying a vertical stress of 16 MPa and holding it fixed. Both Duvaut-Lions and Perzyna formulations predict creep displacements that accelerate with time. For purposes of describing the evolution of the creep-induced shear bands, we select three time instants labeled A, B, and C in Fig. 13, and plot the contours of the norms of the viscoplastic strains at these time instants in Fig. 14. The contours predicted by Duvaut-Lions and Perzyna formulations are nearly identical, so we only show one set of figures in Fig. 14. As in the previous example, the shear band is dilative and propagates in the weaker BN direction. The thickness of the shear band is not constant but appears to grow with time.

Next we consider a shale sample with spatially varying volume fraction. Figure 15 shows the volume fractions for the harder material generated stochastically, assuming uniform distribution from 0.4 to 0.6. The bedding plane orientation for the harder material is the same as before, at $\theta = 45°$. Figure 16 shows the evolution of the vertical displacement at the top of the sample after applying a vertical stress of 15 MPa and holding it fixed. This load is slightly lower than the one used for the homogeneous sample simulation, but Fig. 16 shows that the resulting creep deformation is larger. In general, heterogeneous samples undergo inelastic deformation at an earlier stage than

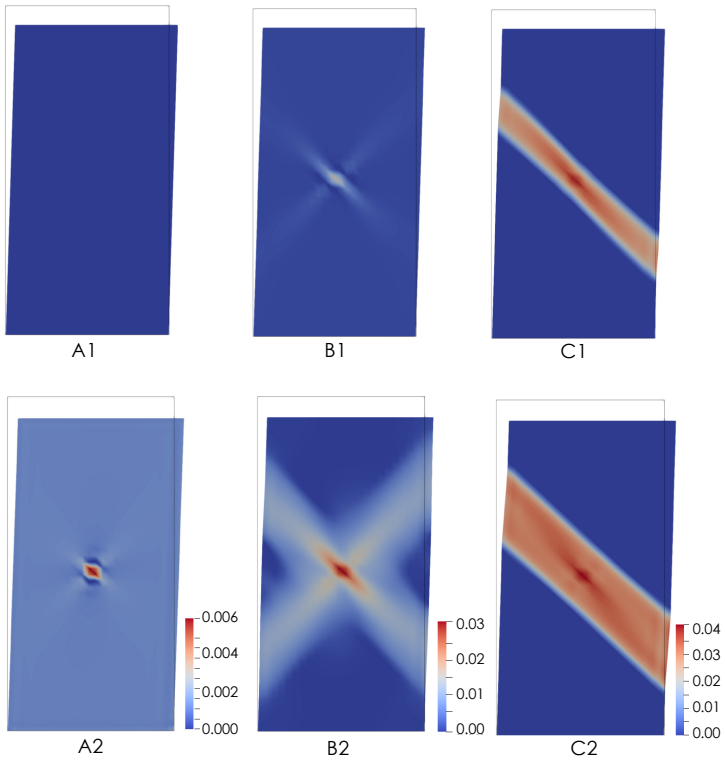

Fig. 11. Cumulative Duvaut-Lions viscoplastic strains. A1 = strain rate A at strain level 1, etc. Color bars are norms of viscoplastic strains in percent. Displacements magnified 200×.

do homogeneous samples due to the more irregular spatial distribution of the stress within the problem domain.

Figures 17 and 18 show multiple creep-induced shear bands at time instants A, B, and C (see Fig. 16 for reference) calculated by Duvaut-Lions and Perzyna viscoplasticity, respectively. The two figures are nearly identical and show an interesting pattern: Shear bands are generally oriented in the weaker BN direction, but smaller shear bands are arranged in phalanx formation aligned with the bedding plane. Note that if there was no anisotropy, one would expect that the smaller shear bands would be randomly positioned and randomly oriented, but not in this particular example where the material possesses cross anisotropy. It is interesting to note that this pattern of shear bands being generally oriented in the BN direction but arranged in phalanx formation in the BP direction could possibly explain why they tend to zigzag along and across bedding planes in cross anisotropic materials, as observed from the experimental results for synthetic transversely isotropic rocks re-

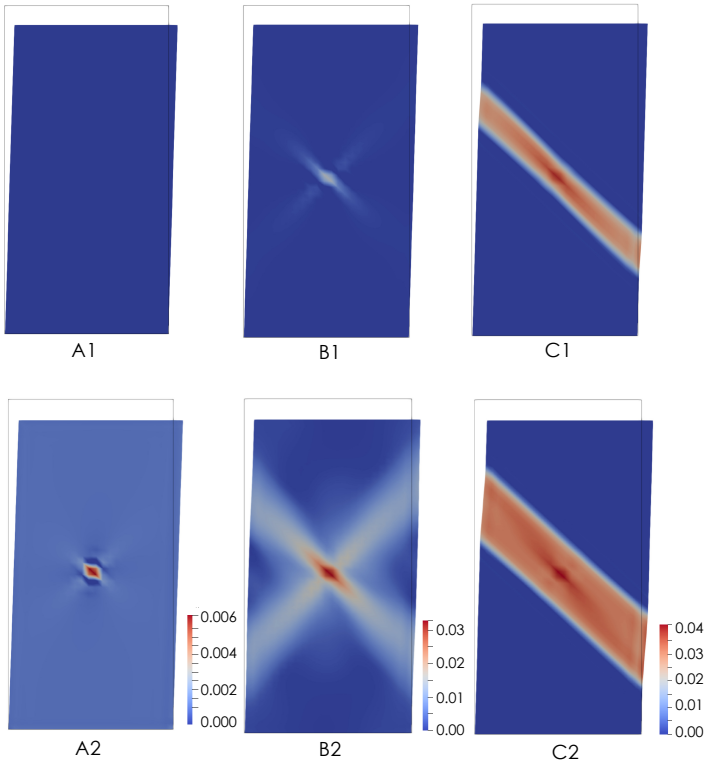

Fig. 12. Cumulative Perzyna viscoplastic strains. A1 = strain rate A at strain level 1, etc. Color bars are norms of viscoplastic strains in percent. Displacements magnified 200×.

ported by Tien et al. [61], for example. For further details on this issue, the readers are referred to Section 5.1 of the recent paper by Zhao et al. [74].

Finally, Fig. 19 shows typical global convergence profiles of Newton-Raphson iterations for the creep problems simulated in this paper. The most number of iterations is 5 during step #1 when the creep strain rate is fastest, then the convergence rate speeds up requiring around 2 iterations only at later stages of the calculations. The Duvaut-Lions calculations take about one more iteration to converge compared to the Perzyna calculations because it needs to compute the elastoplastic closest-point solution, which requires imposing the consistency condition. Given that elastoplasticity is generally 'more nonlinear' compared to viscoplasticity, this observation is not unusual. Other than this minor difference, the two algorithms show comparable rates of convergence.

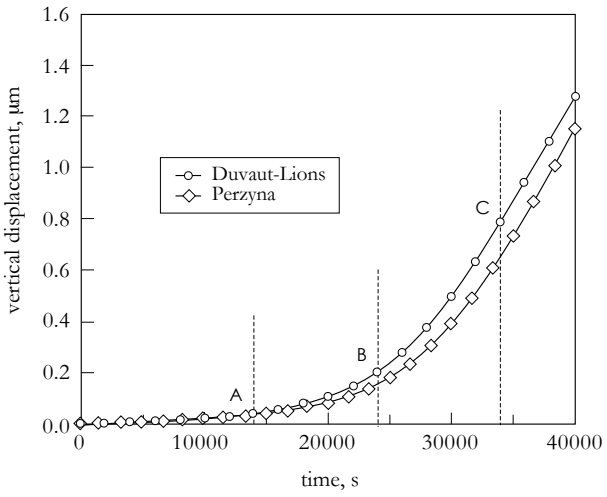

Fig. 13. Creep displacement for a homogeneous shale with one weak element at the center of a rectangular sample.

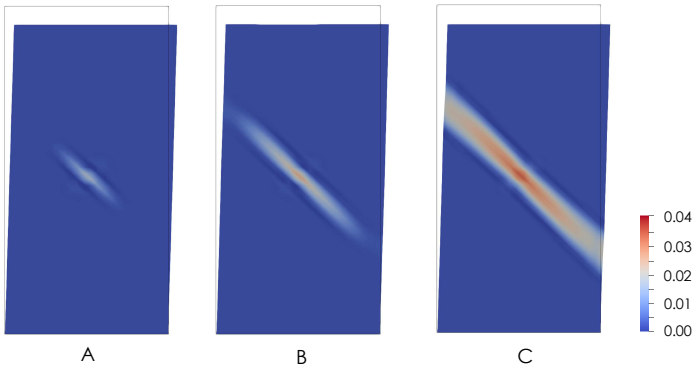

Fig. 14. Evolution of creep-induced dilative shear band for a homogeneous shale with one weak element at the center of a rectangular sample. Plots are nearly identical for Duvaut-Lions and Perzyna simulations. Color bars are norms of viscoplastic strain in percent. Displacements magnified 200×.

4 Closure

We close this paper with a recap of the proposed multiscale framework for shale that accounts for anisotropy, heterogeneity, and rate-dependent effects, as summarized in Fig. 20. The two-material description presented in this paper is a volume-average of the sub-micron scale heterogeneity in a shale. Volume

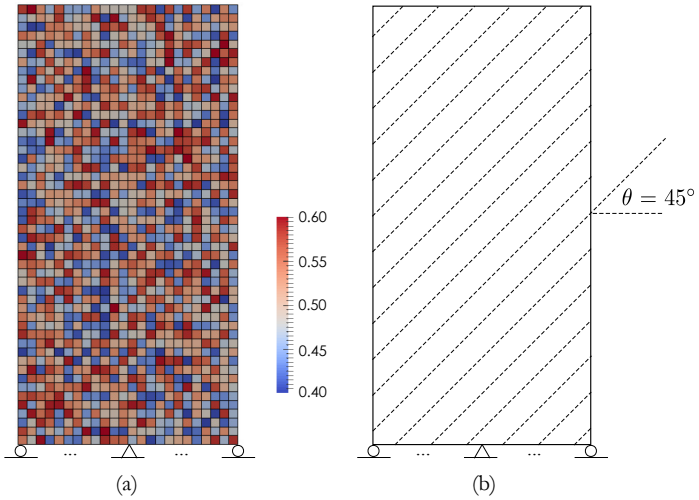

Fig. 15. Simulation of creep process in a heterogeneous shale: (a) stochastically generated volume fraction, and (b) bedding plane orientation for the harder material component.

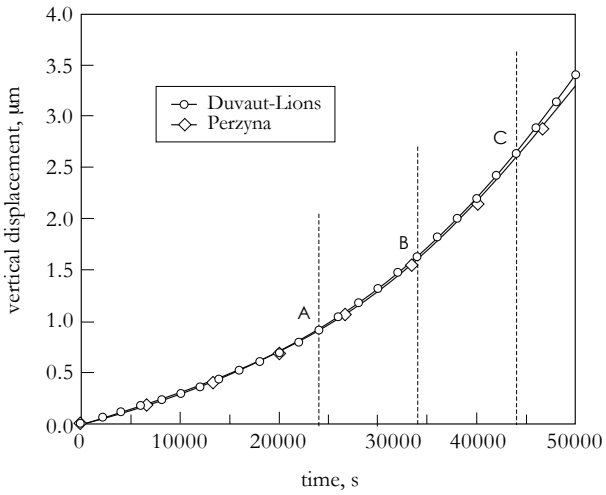

Fig. 16. Creep displacement for a heterogeneous shale with stochastically varying volume fraction.

fractions are the primary variables at the micrometer scale, which could vary from point to point within a millimeter-scale specimen. They can be inferred, for example, from ternary plots obtained from X-ray powder diffraction or

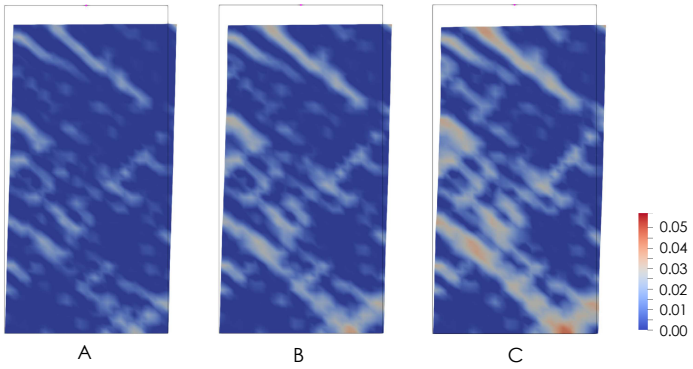

Fig. 17. Evolution of creep-induced shear band in a heterogeneous shale with stochastically varying volume fraction: Duvaut-Lions viscoplasticity (cf. Fig. 16). Color bar is norm of viscoplastic strain in percent. Displacements magnified 200×.

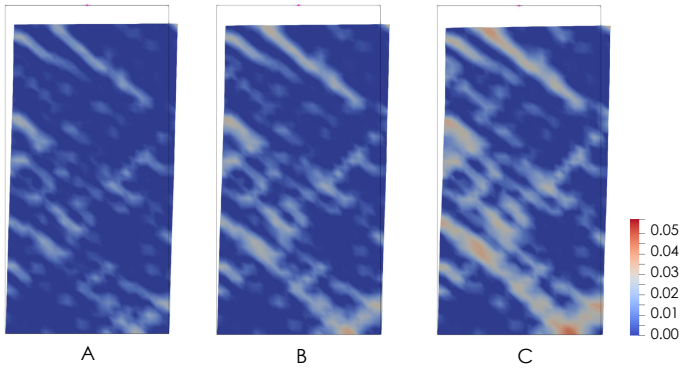

Fig. 18. Evolution of creep-induced shear band in a heterogeneous shale with stochastically varying volume fraction: Perzyna viscoplasticity (cf. Fig. 16). Color bar is norm of viscoplastic strain in percent. Displacements magnified 200×.

some other mineralogy tests. With this setup, we are able to capture two layers of heterogeneity: the nanoscale heterogeneity and the mesoscale heterogeneity, as well as bridge the responses from sub-micron to specimen scales. To our knowledge, no model currently exists for shale that is capable of bridging mechanical processes across such a wide range of scales.

Despite the complex problem being investigated, the framework and model presented in this work are remarkably quite simple. However, validation of the proposed framework against a consistent set of experimental data for the same type of shale is essential, particularly for a model that spans such a wide range of scales. Unfortunately, no data on the mechanical responses of the same type

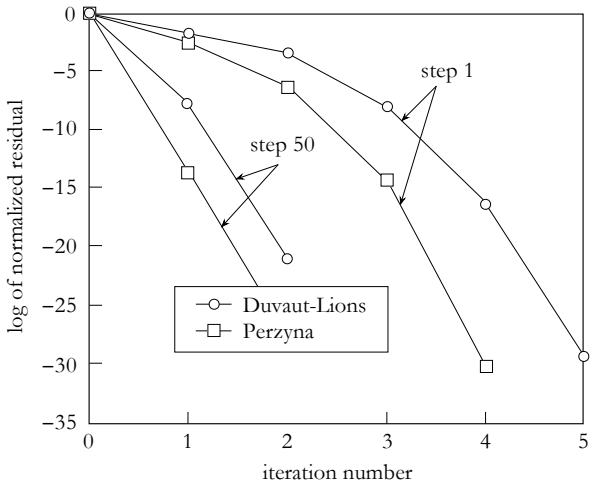

Fig. 19. Convergence profiles of Newton-Raphson iterations for Duvaut-Lions and Perzyna viscoplasticity. Residuals are the Euclidean norms of the out-of-balance nodal force vectors normalized with respect to their initial values at the beginning of the iteration.

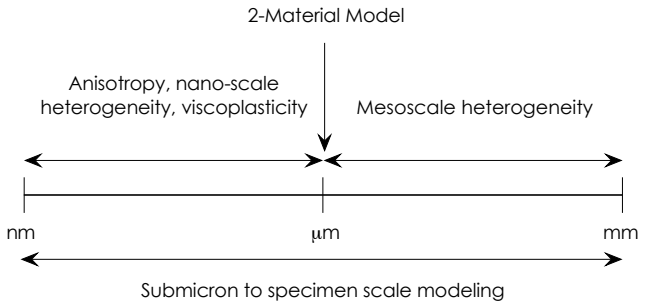

Fig. 20. Recap of two-material modeling of time-dependent deformation behavior of shale showing two layers of heterogeneity: from nanometers to millimeters.

of shale from nanometers to millimeters currently exist in the literature. Work is now underway to generate these much needed data for validation of every aspect of the model presented in this work. Further results will be reported in future publication(s).

Acknowledgments

This work is supported by the U.S. National Science Foundation under Award Number CMMI-1462231 and CMMI-1914780, and by the U.S. Department of Energy, Office of Science, Office of Basic Energy Sciences, Geosciences Research Program, under Award Number DE-FG02-03ER15454.

Appendix A. Perzyna theory – anisotropic version

For brevity, we drop the subscript '$n+1$' and write (19) in residual form

$$\boldsymbol{r}_1 = \boldsymbol{\sigma}_\alpha - \boldsymbol{\sigma}_\alpha^{\mathrm{tr}} + \frac{\Delta t}{\eta_\alpha}\, \boldsymbol{c}_\alpha^e : \Big(f_\alpha \frac{\partial f_\alpha}{\partial \boldsymbol{\sigma}_\alpha} \Big)\,, \tag{36}$$

and also write (33) in residual form

$$r_2 = p_{c\alpha} - p'_{c\alpha}\,, \tag{37}$$

where

$$p'_{c\alpha} = p_{c\alpha,n} \exp\Big(\frac{\Delta t}{\lambda_\alpha^p \eta_\alpha} f_\alpha \frac{\partial f_\alpha}{\partial \boldsymbol{\sigma}_\alpha} : \mathbf{1} \Big) \mathcal{F}(\Theta)\,, \tag{38}$$

assuming $\mathcal{F}(\Theta)$ is given. Symbolically, (36) is a tensor equation, but we can assume it to be vectorized so that the total residual vector may be defined as $\boldsymbol{r}(\boldsymbol{x}) = \{\boldsymbol{r}_1, r_2\}^{\mathsf{T}}$, where $\boldsymbol{x} = \{\boldsymbol{\sigma}_\alpha, p_{c\alpha}\}^{\mathsf{T}}$ is the vectorized set of unknowns. The goal is to determine $\boldsymbol{x}^*$ such that $\boldsymbol{r}(\boldsymbol{x}^*) = \mathbf{0}$. To this end, we employ Newton's method and construct the tangent operator

$$\boldsymbol{r}'(\boldsymbol{x}) = \begin{bmatrix} \boldsymbol{A}_{11} & \boldsymbol{A}_{12} \\ \boldsymbol{A}_{21} & A_{22} \end{bmatrix} = \boldsymbol{A}\,. \tag{39}$$

Note that $\boldsymbol{A}_{11}$ is a 6×6 submatrix for full 3D applications, A_{22} is a scalar field, and $\boldsymbol{A}_{21}$ and $\boldsymbol{A}_{12}$ are row and column vectors, respectively.

We now evaluate the elements of $\boldsymbol{A}$. First, the derivatives of $\boldsymbol{r}_1$ are

$$\boldsymbol{A}_{11} = \frac{\partial \boldsymbol{r}_1}{\partial \boldsymbol{\sigma}_\alpha} = \mathbb{I} + \frac{\Delta t}{\eta_\alpha}\, \boldsymbol{c}_\alpha^e : \Big(f_\alpha \frac{\partial f_\alpha^2}{\partial \boldsymbol{\sigma}_\alpha \partial \boldsymbol{\sigma}_\alpha} + \frac{\partial f_\alpha}{\partial \boldsymbol{\sigma}_\alpha} \otimes \frac{\partial f_\alpha}{\partial \boldsymbol{\sigma}_\alpha} \Big)\,, \tag{40}$$

and

$$\boldsymbol{A}_{12} = \frac{\partial \boldsymbol{r}_1}{\partial p_{c\alpha}} = \frac{\Delta t}{\eta_\alpha}\, \boldsymbol{c}_\alpha^e : \Big(f_\alpha \frac{\partial f_\alpha^2}{\partial \boldsymbol{\sigma}_\alpha \partial p_{c\alpha}} + \frac{\partial f_\alpha}{\partial \boldsymbol{\sigma}_\alpha} \frac{\partial f_\alpha}{\partial p_{c\alpha}} \Big)\,. \tag{41}$$

Next, the derivatives of r_2 are

$$\boldsymbol{A}_{21} = \frac{\partial r_2}{\partial \boldsymbol{\sigma}_\alpha} = -\, p'_{c\alpha} \frac{\Delta t}{\lambda_\alpha^p \eta_\alpha} \Big(f_\alpha \frac{\partial^2 f_\alpha}{\partial \boldsymbol{\sigma}_\alpha \partial \boldsymbol{\sigma}_\alpha} + \frac{\partial f_\alpha}{\partial \boldsymbol{\sigma}_\alpha} \otimes \frac{\partial f_\alpha}{\partial \boldsymbol{\sigma}_\alpha} \Big) : \mathbf{1}\,, \tag{42}$$

and

$$A_{22} = \frac{\partial r_2}{\partial p_{c\alpha}} = 1 - p'_{c\alpha}\frac{\Delta t}{\lambda^p_\alpha \eta_\alpha}\Big(f_\alpha \frac{\partial f^2_\alpha}{\partial \boldsymbol{\sigma}_\alpha \partial p_{c\alpha}} + \frac{\partial f_\alpha}{\partial \boldsymbol{\sigma}_\alpha}\frac{\partial f_\alpha}{\partial p_{c\alpha}}\Big) : \mathbf{1}\,. \tag{43}$$

At the conclusion of the local Newton iteration, we know that

$$\boldsymbol{r}(\boldsymbol{x}^*, \boldsymbol{\epsilon}) = \mathbf{0} \tag{44}$$

for a given $\boldsymbol{\epsilon}$. Thus, differentiating with respect to $\boldsymbol{\epsilon}$ at the locally converged configuration $\boldsymbol{x}^*$ gives

$$\frac{\partial \boldsymbol{r}}{\partial \boldsymbol{\epsilon}} = \boldsymbol{b} + \boldsymbol{A}^* \frac{\partial \boldsymbol{x}}{\partial \boldsymbol{\epsilon}} = \mathbf{0}\,, \tag{45}$$

where

$$\boldsymbol{b} = \Big(\frac{\partial \boldsymbol{r}}{\partial \boldsymbol{\epsilon}}\Big)_{\boldsymbol{x}=\text{fixed}} = \begin{pmatrix} -\boldsymbol{c}^e \\ \mathbf{0} \end{pmatrix}, \tag{46}$$

and $\boldsymbol{A}^*$ is the value of $\boldsymbol{A}$ evaluated at the converged local configuration $\boldsymbol{x}^*$. This gives

$$\frac{\partial \boldsymbol{x}}{\partial \boldsymbol{\epsilon}} = \begin{pmatrix} \partial \boldsymbol{\sigma}_\alpha / \partial \boldsymbol{\epsilon} \\ \partial p_{c\alpha} / \partial \boldsymbol{\epsilon} \end{pmatrix} = -\boldsymbol{A}^{*-1}\boldsymbol{b}\,. \tag{47}$$

The last equation determines the algorithmic stress-strain moduli tensor $\boldsymbol{c}_{\alpha,n+1} = \partial \boldsymbol{\sigma}_\alpha / \partial \boldsymbol{\epsilon}$ for the Perzyna viscoplastic model. □

Appendix B. Perzyna theory – isotropic version

We note that the isotropic case can be recovered from the anisotropic theory simply by setting the anisotropy parameters to their appropriate values. However, implementing the isotropic theory separately may be warranted for some large-scale calculations because it generally results in much improved efficiency, as can be seen from the formulations below.

The key here is to work with the first two stress invariants $p = \text{tr}(\boldsymbol{\sigma})/3$ and $q = \sqrt{3/2}\|\boldsymbol{s}\|$, where $\boldsymbol{s} = \text{dev}(\boldsymbol{\sigma})$; and the first two strain invariants $\varepsilon_v = \text{tr}(\boldsymbol{\epsilon})$ and $\varepsilon_s = \sqrt{2/3}\|\boldsymbol{e}\|$, where $\boldsymbol{e} = \text{dev}(\boldsymbol{\epsilon})$, see [15]. Converting (34) to residual form gives

$$\left.\begin{aligned} r_1 &= p - p^{\text{tr}} + K\frac{\Delta t}{\eta}\Big(f\frac{\partial f}{\partial p}\Big) \\ r_2 &= q - q^{\text{tr}} + 3\mu\frac{\Delta t}{\eta}\Big(f\frac{\partial f}{\partial q}\Big) \\ r_3 &= p_c - p'_c \end{aligned}\right\}, \tag{48}$$

where K and μ are the elastic bulk and shear moduli, respectively, and

$$p'_c = p_{cn}\exp\Big[\frac{\Delta t}{\lambda^p \eta}\Big(f\frac{\partial f}{\partial p}\Big)\Big]\mathcal{F}(\Theta)\,. \tag{49}$$

The unknowns are $x_1 = p$, $x_2 = q$, and $x_3 = p_c$. We want to find $\boldsymbol{x}^*$ such that $\boldsymbol{r}(\boldsymbol{x}^*) = \boldsymbol{0}$, so we use Newton's method and construct the tangent operator $\boldsymbol{A} = \boldsymbol{r}'(\boldsymbol{x})$. For r_1, the derivatives are:

$$\left.\begin{aligned} A_{11} &= 1 + K\frac{\Delta t}{\eta}\Big[f\frac{\partial^2 f}{\partial p^2} + \Big(\frac{\partial f}{\partial p}\Big)^2\Big] \\ A_{12} &= K\frac{\Delta t}{\eta}\Big(\frac{\partial f}{\partial p}\frac{\partial f}{\partial q}\Big) \\ A_{13} &= K\frac{\Delta t}{\eta}\Big(f\frac{\partial^2 f}{\partial p \partial p_c} + \frac{\partial f}{\partial p}\frac{\partial f}{\partial p_c}\Big) \end{aligned}\right\}. \tag{50}$$

For r_2, the derivatives are:

$$\left.\begin{aligned} A_{21} &= 3\mu\frac{\Delta t}{\eta}\Big(\frac{\partial f}{\partial q}\frac{\partial f}{\partial p}\Big) \\ A_{22} &= 1 + 3\mu\frac{\Delta t}{\eta}\Big[f\frac{\partial^2 f}{\partial q^2} + \Big(\frac{\partial f}{\partial q}\Big)^2\Big] \\ A_{23} &= 3\mu\frac{\Delta t}{\eta}\Big(f\frac{\partial^2 f}{\partial q \partial p_c} + \frac{\partial f}{\partial q}\frac{\partial f}{\partial p_c}\Big) \end{aligned}\right\}. \tag{51}$$

And for r_3, the derivatives are:

$$\left.\begin{aligned} A_{31} &= -p_c'\frac{\Delta t}{\lambda^p \eta}\Big[f\frac{\partial^2 f}{\partial p^2} + \Big(\frac{\partial f}{\partial p}\Big)^2\Big] \\ A_{32} &= -p_c'\frac{\Delta t}{\lambda^p \eta}\Big(\frac{\partial f}{\partial p}\frac{\partial f}{\partial q}\Big) \\ A_{33} &= 1 - p_c'\frac{\Delta t}{\lambda^p \eta}\Big(f\frac{\partial^2 f}{\partial p \partial p_c} + \frac{\partial f}{\partial p}\frac{\partial f}{\partial p_c}\Big) \end{aligned}\right\}. \tag{52}$$

At the conclusion of the iteration, we obtain the roots p and q (as well as p_c), from which we construct the full Cauchy stress tensor as indicated in (35). To obtain the algorithmic stress-strain moduli tensor, we differentiate (35) directly as follows

$$\begin{aligned} \boldsymbol{c} = \frac{\partial \boldsymbol{\sigma}}{\partial \boldsymbol{\epsilon}} = \boldsymbol{1} \otimes \Big(D_{11}\frac{\partial \varepsilon_v}{\partial \boldsymbol{\epsilon}} + D_{12}\frac{\partial \varepsilon_s}{\partial \boldsymbol{\epsilon}}\Big) + \sqrt{\frac{2}{3}}\hat{\boldsymbol{n}} \otimes \Big(D_{21}\frac{\partial \varepsilon_v}{\partial \boldsymbol{\epsilon}} + D_{22}\frac{\partial \varepsilon_s}{\partial \boldsymbol{\epsilon}}\Big) \\ + \frac{2q}{3\varepsilon_s}\Big(\mathbb{I} - \frac{1}{3}\boldsymbol{1} \otimes \boldsymbol{1} - \hat{\boldsymbol{n}} \otimes \hat{\boldsymbol{n}}\Big), \end{aligned} \tag{53}$$

where

$$D_{11} = \frac{\partial p}{\partial \varepsilon_v}, \quad D_{12} = \frac{\partial p}{\partial \varepsilon_s}, \quad D_{21} = \frac{\partial q}{\partial \varepsilon_v}, \quad D_{22} = \frac{\partial q}{\partial \varepsilon_s}. \tag{54}$$

Note that $\partial \varepsilon_v / \partial \boldsymbol{\epsilon} = \boldsymbol{1}$ and $\partial \varepsilon_s / \partial \boldsymbol{\epsilon} = \sqrt{2/3}\,\hat{\boldsymbol{n}}$, so the algorithmic stress-strain moduli tensor simplifies to

$$\boldsymbol{c} = \frac{2q}{3\varepsilon_s}\big(\mathbb{I} - \hat{\boldsymbol{n}} \otimes \hat{\boldsymbol{n}}\big) + \Big(D_{11} - \frac{2q}{9\varepsilon_s}\Big)\mathbf{1} \otimes \mathbf{1} + \frac{2}{3}D_{22}\hat{\boldsymbol{n}} \otimes \hat{\boldsymbol{n}} + \sqrt{\frac{2}{3}}\Big(D_{12}\mathbf{1} \otimes \hat{\boldsymbol{n}} + D_{21}\hat{\boldsymbol{n}} \otimes \mathbf{1}\Big)\,. \tag{55}$$

To determine the D_{ij}'s, we note that

$$r_i(x_j, \varepsilon_k) = 0\,, \qquad i,j = 1,2,3\,; \quad k = v, s \tag{56}$$

when evaluated at the converged configuration x_j^*. So, at the converged configuration we have

$$\frac{\partial r_i}{\partial \varepsilon_k} = \underbrace{\frac{\partial r_i}{\partial x_j}}_{A_{ij}} \frac{\partial x_j}{\partial \varepsilon_k} + \underbrace{\frac{\partial r_i}{\partial \varepsilon_k}}_{B_{ik}}\Big|_{x_j = \text{fixed}} = 0\,, \tag{57}$$

where

$$\frac{\partial r_i}{\partial \varepsilon_k}\Big|_{x_j = \text{fixed}} = B_{ik} \tag{58}$$

and

$$[B_{ik}] = \begin{bmatrix} -K & 0 \\ 0 & -3\mu \\ 0 & 0 \end{bmatrix}\,. \tag{59}$$

Solving gives

$$\frac{\partial x_j}{\partial \varepsilon_k} = -A_{ji}^{-1} B_{ik}\,. \tag{60}$$

Note that $D_{jk} = \partial x_j / \partial \varepsilon_k$ for $j = 1, 2$ and $k = v, s$. □

References

[1] J.F. Abel Jr., F.T. Lee (1980). Subsidence potential in shale and crystalline rocks. United States Department of the Interior Geological Survey, Open-File Report 80-1072.

[2] J.E. Andrade, R.I.Borja (2006). Capturing strain localization in dense sands with random density. International Journal for Numerical Methods in Engineering 67:1531–1564.

[3] I.O. Bayuk, I. O., M. Ammerman, M., E.M. Chesnokov, E. M. (2007). Elastic moduli of anisotropic clay. Geophysics, 72(5): D107-D117.

[4] B.P. Belikov, K.S. Aleksandrov, T.V. Ryzhova (1970). Elastic properties of rock-forming minerals and rocks. Moscow: Nauka.

[5] R.H. Bennett, N.R. O'Brien, M.H. Hulbert (1991). Determinants of clay and shale microfabric signatures: Processes and mechanisms, In: R.H. Bennett, W.R. Bryant and M.H. Hulbert (Eds.), Microstructure of Fine-Grained Sediments: From Mud to Shale, Springer-Verlag, New York.

[6] K.C. Bennett, R.I. Borja (2018). Hyper-elastoplastic/damage modeling of rock with application to porous limestone. International Journal of Solids and Structures 143:218–231.
[7] K.C. Bennett, R.A. Regueiro, R.I. Borja (2016). Finite strain elastoplasticity considering the Eshelby stress for materials undergoing plastic volume change. International Journal of Plasticity 77:214–245.
[8] K.C. Bennett, L. Berla, R.I. Borja, W.D. Nix (2015). Instrumented nanoindentation and 3D mechanistic modeling of a shale at multiple scales. Acta Geotechnica 10:1–14.
[9] L. Bjerrum (1967). Engineering geology of Norwegian normally consolidated marine clays as related to settlements of buildings. 7th Rankine Lecture, Géotechnique 17:83–117.
[10] J.P. Boehler, A. Sawczuk (1977). On yielding of oriented solids. Acta Mechanica 27:185–206.
[11] R.I. Borja, J. Choo (2016). Cam-Clay plasticity. Part VIII: A constitutive framework for porous materials with evolving internal structure. Computer Methods in Applied Mechanics and Engineering 309:653–679.
[12] R.I. Borja (2013). Plasticity Modeling & Computation. Springer, Berlin-Heidelberg.
[13] R.I. Borja, X. Song, A.L. Rechenmacher, S. Abedi, W. Wu (2013). Shear band in sand with spatially varying density, Journal of the Mechanics and Physics of Solids 61:219–234.
[14] R.I. Borja, X. Song, W. Wu (2013). Critical state plasticity, Parti VII: Triggering a shear band in variably saturated porous media. Computer Methods in Applied Mechanics and Engineering 261–262:66–82.
[15] R.I. Borja (1990). Cam-Clay plasticity, Part 1: Implicit integration of elasto-plastic constitutive relations. Computer Methods in Applied Mechanics and Engineering 78:49–72.
[16] R.I. Borja, E. Kavazanjian Jr. (1985). A constitutive model for the stress-strain-time behaviour of 'wet' clays. Géotechnique 35, 283–298.
[17] E.C. Bryant, W.C. Sun (2018). A mixed-mode phase field fracture model in anisotropic rocks with consistent kinematics. Computer Methods in Applied Mechanics and Engineering 342:561–568.
[18] E.C. Bryant, W.C. Sun (2019). A micromorphically regularized Cam-clay model for capturing size-dependent anisotropy of geomaterials. Computer Methods in Applied Mechanics and Engineering 354:56–95.
[19] H. M. Celleri, M. Sánchez, J. L. Otegui (2018). Fracture behavior of transversely isotropic rocks with discrete weak interfaces, International Journal for Numerical and Analytical Methods in Geomechanics 42 (2018) 2161–2176.
[20] C. Chang, M.D. Zoback (2009). Viscous creep in room-dried unconsolidated Gulf of Mexico shale (I): Experimental results. Journal of Petroleum Science and Engineering 69:239–246.
[21] C. Chang, M.D. Zoback (2008). Creep in unconsolidated shale and its implications on rock physical properties. Paper presented at the 42th US

Rock Mechanics Symposium and 2nd US-Canada Rock Mechanics Symposium, San Francisco, June 29-July 2, 2008, Paper No. ARMA 08-130.

[22] L. Chen, J.F. Shao, Q.Z. Zhu, G. Duveau (2012). Induced anisotropic damage and plasticity in initially anisotropic sedimentary rocks, International Journal of Rock Mechanics and Mining Sciences 51, 13–23.

[23] J. Choo, R.I. Borja (2016). Stabilized mixed finite elements for deformable porous media with double porosity. Computer Methods in Applied Mechanics and Engineering 293:131–154.

[24] J. Choo, J.A. White, R.I. Borja (2016). Hydromechanical modeling of unsaturated flow in double porosity media. International Journal of Geomechanics, DOI: 10.1061/(ASCE)GM.1943-5622.0000558, D4016002.

[25] J. Choo, W.C. Sum (2018). Coupled phase-field and plasticity modeling of geological materials: From brittle fracture to ductile flow. Computer Methods in Applied Mechanics and Engineering 330: 1–32.

[26] J. Choo, W.C. Sum (2018). Cracking and damage from crystallization in pores: Coupled chemo-hydro-mechanics and phase-field modeling. Computer Methods in Applied Mechanics and Engineering 335: 347–379.

[27] R.J. Day-Stirrat, S.P. Dutton, K.L. Millken, R.G. Loucks, A.C. Aplin, S. Hillier, B.A. van der Pluijm (2010). Fabric anisotropy induced by primary depositional variations in the silt: clay ratio in two fine-grained slope fan complexes: Texas Gulf Coast and northern North Sea. Sedimentary Geology 226, 42–53.

[28] M.B. Dusseault, C.J. Fordham (1993). Time-dependent behavior of rocks. Comprehensive Rock Engineering Principles, Practice & Project: Rock Testing and Site Characterization 3:119–149.

[29] G. Duvaut, J.L. Lions (1976). Inequalities in Mechanics and Physics, Springer-Verlag, Berlin-Heidelberg.

[30] A.H. Fávero Neto, R.I. Borja (2018). Continuum hydrodynamics of dry granular flows employing multiplicative elastoplasticity. Acta Geotechnica 13:1027–1040.

[31] Z.L. Fu, Y.F. Ning, J.P. Xu (2007). Creep of anisotropic oil shale. Journal of Mining and Safety Engineering 24:353–356.

[32] R. Hill (1963). Elastic properties of reinforced solids: Some theoretical principles. Journal of the Mechanics and Physics of Solids 11:357–372.

[33] P. Horsrud, R. Holt, E. Sonstebo, G. Svano, B. Bostrom (1994). Time dependent borehole stability: Laboratory studies and numerical simulation of different mechanisms in shale. Rock Mechanics in Petroleum Engineering, Society of Petroleum Engineers, 29–31 August 1994, Delft, Netherlands.

[34] R.L. Ingram (1953). Fissility of Mudrocks, Bulletin of the Geological Society of America 64, 869–878.

[35] L. Laloui, C. Cekerevac (2003) Thermo-plasticity of clays: an isotropic yield mechanism. Computers and Geotechnics 30:649–660.

[36] G. Lash, T. Engelder (2005). An analysis of horizontal microcracking during catagenesis: Example from the Catskill delta complex, The American Association of Petroleum Geologists 89, 1433–1449.

[37] M. Lazari, L. Sanavia, C. di Prisco, F. Pisano (2019). Predictive potential of Perzyna viscoplastic modelling for granular geomaterials. International Journal for Numerical and Analytical Methods in Geomechanics 43:544–567.

[38] S.Y. Lee, L.K. Hyder, P.D. Alley (1991). Microstructural and mineralogical characterization of selected shales in support of nuclear waste repository studies, In: R.H. Bennett, W.R. Bryant and M.H. Hulbert (Eds.), Microstructure of Fine-Grained Sediments: From Mud to Shale, Springer-Verlag, New York.

[39] I. Lonardelli, H. Wenk, Y. Ren (2007). Preferred orientation and elastic anisotropy in shales, Geophysics 72, D33–D40.

[40] R. Namani, Y. Feng, R.J. Okamoto, N Jesuraj, S.E. Sakiyama-Elbert, G.M. Genin, P.V. Bayly (2012). Elastic characterization of transversely isotropic soft materials by dynamic shear and asymmetric indentation. Journal of Biomechanical Engineering, 134(6): 061004.

[41] H. Niandou, J.F. Shao, J.P. Henry, D. Fourmaintraux D (1997) Laboratory investigation of the mechanical behaviour of Tournemire shale. International Journal of Rock Mechanics and Mining Sciences 34(1):3–16

[42] F. Oka, T. Adachi, A. Yashima (1994). Instability of an elasto-viscoplastic constitutive model for clay and strain localization. Mechanics of Materials 18:119–129.

[43] J.A. Ortega, F.-J. Ulm, Y. Abousleiman (2010). The effect of particle shape and grain-scale properties of shale: A micromechanics approach. International Journal for Numerical and Analytical Methods in Geomechanics 34, 1124–1156.

[44] P. Perzyna (1966). Fundamental problems in viscoplasticity. Advances in Applied Mechanics 9:244–368.

[45] F.J. Pettijohn (1975). Sedimentary Rocks, Third Edition, Harper and Row Publishers, New York, N.Y.

[46] C.D. Piane, D.N. Dewhurst, A.F. Siggins, M.D. Raven (2011). Stress-induced anisotropy in brine saturated shale, Geophysical Journal International 184, 897–906.

[47] R. Quevedo, P. Firme, D. Roehl (2019). Integration schemes with substepping algorithms for creep analysis in geomaterials. International Journal for Numerical and Analytical Methods in Geomechanics 43:1467–1487.

[48] R. Risnes (2008). Petroleum Related Rock Mechanics, 2nd Edition, Elsevier.

[49] T. Saksala (2019). Numerical modeling of adiabatic heat generation during rock fracture under dynamic loading. International Journal for Numerical and Analytical Methods in Geomechanics 43:1770–1783.

[50] L.E. Schwer (1994). Viscoplastic augmentation of the smooth cap model. Nuclear Engineering and Design 150:215–223.

[51] S.J. Semnani, R.I. Borja (2017). Quantifying the heterogeneity of shale through statistical combination of imaging across scales. Acta Geotechnica 12:1193–1205.

[52] S.J. Semnani, J.A. White, R.I. Borja (2016). Thermo-plasticity and strain localization in transversely isotropic materials based on anisotropic critical state plasticity. International Journal for Numerical and Analytical Methods in Geomechanics 40:2423–2449.

[53] J.C. Simo, T.J.R. Hughes (1998). Computational Inelasticity. Springer-Verlag, Berlin-Heidelberg.

[54] M. Slim, S. Abedi, L.T. Bryndzia, F.-J. Ulm (2019). Role of organic matter on nanoscale and microscale creep properties of source rocks. Journal of Engineering Mechanics 145(1): 04018121, https://doi.org/10.1061/(ASCE)EM.1943-7889.0001538

[55] H. Sone, M.D. Zoback (2010). Strength, creep and frictional properties of gas shale reservoir rocks. Proceedings of the 44th US Rock Mechanics Symposium and 5th US-Canada Rock Mechanics Symposium, June.

[56] H. Sone, M.D. Zoback (2011). Visco-plastic properties of shale gas reservoir rocks. Proceedings of the 45th US Rock Mechanics/Geomechanics Symposium, June.

[57] H. Sone, M.D. Zoback (2013). Mechanical properties of shale-gas reservoir rocks – Part 1: Static and dynamic elastic properties and anisotropy. Geophysics 78, D381–D392.

[58] H. Sone, M.D. Zoback (2013). Mechanical properties of shale-gas reservoir rocks – Part 2: Ductile creep, brittle strength, and their relation to the elastic modulus. Geophysics 78, D393–D402.

[59] X. Song, R.I. Borja (2014). Mathematical framework for unsaturated flow in the finite deformation range. International Journal for Numerical Methods in Engineering 97:658–682.

[60] X. Song, R.I. Borja (2014). Finite deformation and fluid flow in unsaturated soil with random heterogeneity. Vadose Zone Journal 13(5), doi:10.2136/vzj2013.07.0131.

[61] Y.M. Tien, M.C. Kuo, and C.H. Juang (2006). An experimental investigation of the failure mechanism of simulated transversely isotropic rocks. International Journal of Rock Mechanics and Mining Sciences 43:1163–1181.

[62] M. Tjioe, R.I. Borja (2015). On the pore-scale mechanisms leading to brittle and ductile deformation behavior of crystalline rocks. International Journal for Numerical and Analytical Methods in Geomechanics 39:1165–1187

[63] M. Tjioe, R.I. Borja (2016). Pore-scale modeling of deformation and shear band bifurcation in porous crystalline rocks. International Journal for Numerical Methods in Engineering 108:183–212.

[64] F.-J. Ulm, Y. Abousleiman (2006). The nanogranular nature of shale, Acta Geotechnica 1:77–88.

[65] S.L.A. Valcke, M. Casey, G.E. Lloyd, J. Kendall, Q.J. Fisher (2006). Lattice preferred orientation and seismic anisotropy in sedimentary rocks. Geophysical Journal International 166, 652–666.

[66] L. Vernik (1994). Hydrocarbon-generation-induced microcracking of source rocks, Geophysics 59:555–563.

[67] J.G. Wang, B. Liang (2010). Creep characteristics analysis of oil shale and its application. Applied Mechanics and Materials 29:2614–2619.

[68] H.R. Wenk, M. Voltolini, M. Mazurek, L.R. Van Loon, A. Vinsot (2008). Preferred orientations and anisotropy in shales: Callovo-Oxfordian shale (France) and Opalinus clay (Switzerland), Clays and Clay Minerals 56:285–306.

[69] R.C.K. Wong, R.D. Schmitt, D. Collins, R. Gautam (2008). Inherent transversely isotropic elastic parameters of over-consolidated shale measured by ultrasonic waves and their comparison with static and acoustic *in situ* log measurements. Journal of Geophysics and Engineering 5:103–117.

[70] M. Xu, D. Jin, E. Song, D. Shen (2018). A rheological model to simulate the shear creep behavior of rockfills considering the influence of stress states. Acta Geotechnica 13:1313–1327.

[71] Z.-Y. Yin, Y.-F. Jin, S.-L. Shen, H.-W. Huang (2017). An efficient optimization method for identifying parameters of soft structured clay by an enhanced genetic algorithm and elastic-viscoplastic model. Acta Geotechica 12:849–867.

[72] Q. Zhang, J. Choo, R.I. Borja (2019). On the preferential flow patterns induced by transverse isotropy and non-Darcy flow in double porosity media. Computer Methods in Applied Mechanics and Engineering 352, DOI: https://doi.org/10.1016/j.cma.2019.04.037

[73] Y. Zhao, R.I. Borja (2019). Deformation and strength of transversely isotropic rocks. In: (W. Wu, Ed.) Desiderata Geotechnica, Springer Nature, Switzerland AG, pp. 237–241.

[74] Y. Zhao, S.J. Semnani, Q. Yin, R.I. Borja (2018). On the strength of transversely isotropic rocks. International Journal for Numerical and Analytical Methods in Geomechanics 42:1917–1934.

[75] D. Zhao, M. Hattab, Z.-Y. Yin, P.-Y. Hicher (2019). Dilative behavior of kaolinite under drained creep condition. Acta Geotechnica 14:1003–1019.

[76] S. Zou, J. Li, X. Xie, Z. Wang (2019). Study of the 1-D consolidation behavior of two?layered soft soils: Parametric studies using a rheological model with viscoplastic body. International Journal for Numerical and Analytical Methods in Geomechanics 43:501–518.